A Search for Persistent Radio Sources toward Repeating Fast Radio Bursts Discovered by CHIME/FRB

The Astrophysical Journal, 976:199 (30pp), 2024 December 1 https://doi.org/10.3847/1538-4357/ad808e

A Search for Persistent Radio Sources toward Repeating Fast Radio Bursts Discovered by CHIME/FRB

Adaeze L. Ibik[1,2], Maria R. Drout[2], B. M. Gaensler[1,2,3], Paul Scholz[1,4], Navin Sridhar[5,6], Ben Margalit[7], T. E. Clarke[8], Casey J. Law[6,9], Shriharsh P. Tendulkar[10,11,12], Daniele Michilli[13,14], Tarraneh Eftekhari[15], Mohit Bhardwaj[16], Sarah Burke-Spolaor[17,18], Shami Chatterjee[19], Amanda M. Cook[1,2], Jason W. T. Hessels[20,21,22,23], Franz Kirsten[23,24], Ronniy C. Joseph[20,21], Victoria M. Kaspi[20,21], Mattias Lazda[1,2], Kiyoshi W. Masui[13,14], Kenzie Nimmo[13], Ayush Pandhi[1,2], Aaron B. Pearlman[20,21], Ziggy Pleunis[1,22,23], Masoud Rafiei-Ravandi[20,21], Kaitlyn Shin[13,14], and Kendrick M. Smith[25]

[1] Dunlap Institute for Astronomy & Astrophysics, University of Toronto, 50 St. George Street, Toronto, ON M5S 3H4, Canada; adaeze.ibik@mail.utoronto.ca
[2] David A. Dunlap Department of Astronomy & Astrophysics, University of Toronto, 50 St. George Street, Toronto, ON M5S 3H4, Canada
[3] Department of Astronomy and Astrophysics, University of California Santa Cruz, 1156 High Street, Santa Cruz, CA 95064, USA
[4] Department of Physics and Astronomy, York University, 4700 Keele Street, Toronto, Ontario, ON MJ3 1P3, Canada
[5] Department of Astronomy, Columbia University, New York, NY 10027, USA
[6] Cahill Center for Astronomy and Astrophysics, MC 249-17 California Institute of Technology, Pasadena, CA 91125, USA
[7] School of Physics and Astronomy, University of Minnesota, Minneapolis, MN 55455, USA
[8] Naval Research Laboratory, Code 7213, 4555 Overlook Avenue SW, Washington, DC 20375, USA
[9] Owens Valley Radio Observatory, California Institute of Technology, Big Pine, CA 93513, USA
[10] Department of Astronomy and Astrophysics, Tata Institute of Fundamental Research, Mumbai, 400005, India
[11] National Centre for Radio Astrophysics, Post Bag 3, Ganeshkhind, Pune, 411007, India
[12] CIFAR Azrieli Global Scholars Program, CIFAR, Toronto, Canada
[13] MIT Kavli Institute for Astrophysics and Space Research, Massachusetts Institute of Technology, 77 Massachusetts Avenue, Cambridge, MA 02139, USA
[14] Department of Physics, Massachusetts Institute of Technology, 77 Massachusetts Avenue, Cambridge, MA 02139, USA
[15] Center for Interdisciplinary Exploration and Research in Astrophysics (CIERA) and Department of Physics and Astronomy, Northwestern University, Evanston, IL 60208, USA
[16] Department of Physics, Carnegie Mellon University, 5000 Forbes Avenue, Pittsburgh, PA 15213, USA
[17] Department of Physics and Astronomy, West Virginia University, P.O. Box 6315, Morgantown, WV 26506, USA
[18] Center for Gravitational Waves and Cosmology, West Virginia University, Chestnut Ridge Research Building, Morgantown, WV 26505, USA
[19] Department of Astronomy and Cornell Center for Astrophysics and Planetary Science, Cornell University, Ithaca, NY 14853, USA
[20] Department of Physics, McGill University, 3600 rue University, Montréal, QC H3A 2T8, Canada
[21] Trottier Space Institute, McGill University, 3550 rue University, Montréal, QC H3A 2A7, Canada
[22] Anton Pannekoek Institute for Astronomy, University of Amsterdam, Science Park 904, 1098 XH Amsterdam, The Netherlands
[23] ASTRON, Netherlands Institute for Radio Astronomy, Oude Hoogeveensedijk 4, 7991 PD Dwingeloo, The Netherlands
[24] Department of Space, Earth and Environment, Chalmers University of Technology, Onsala Space Observatory, 439 92, Onsala, Sweden
[25] Perimeter Institute for Theoretical Physics, 31 Caroline Street N, Waterloo, ON N25 2YL, Canada
Received 2024 July 15; revised 2024 September 17; accepted 2024 September 24; published 2024 November 22

Abstract

The identification of persistent radio sources (PRSs) coincident with two repeating fast radio bursts (FRBs) supports FRB theories requiring a compact central engine. However, deep nondetections in other cases highlight the diversity of repeating FRBs and their local environments. Here, we perform a systematic search for radio sources towards 37 CHIME/FRB repeaters using their arcminute localizations and a combination of archival surveys and targeted observations. Through multiwavelength analysis of individual radio sources, we identify two (20181030A-S1 and 20190417A-S1) for which we disfavor an origin of either star formation or an active galactic nucleus in their host galaxies and thus consider them candidate PRSs. We do not find any associated PRSs for the majority of the repeating FRBs in our sample. For eight FRB fields with Very Large Array imaging, we provide deep limits on the presence of PRSs that are 2–4 orders of magnitude fainter than the PRS associated with FRB 20121102A. Using Very Large Array Sky Survey imaging of all 37 fields, we constrain the rate of luminous ($\gtrsim 10^{40}$ erg s^{-1}) PRSs associated with repeating FRBs to be low. Within the context of FRB-PRS models, we find that 20181030A-S1 and 20190417A-S1 can be reasonably explained within the context of magnetar, hypernebulae, gamma-ray burst afterglow, or supernova ejecta models—although we note that both sources follow the radio luminosity versus rotation measure relationship predicted in the nebula model framework. Future observations will be required to both further characterize and confirm the association of these PRS candidates with the FRBs.

Unified Astronomy Thesaurus concepts: Radio transient sources (2008); Radio sources (1358); Transient sources (1851)

1. Introduction

More than 750 short-duration energetic radio transients, known as fast radio bursts (FRBs; D. R. Lorimer et al. 2007), have been reported to date (e.g., CHIME/FRB Collaboration et al. 2021; K. Nimmo et al. 2023). There are two apparent populations of FRBs: "one-off" FRBs and "FRB repeaters," the

latter of which have shown more than one burst. While only accounting for <10% of known FRBs (CHIME/FRB Collaboration et al. 2021; D. Michilli et al. 2023; CHIME/FRB Collaboration & B. C. Andersen 2023), repeaters are particularly interesting since they provide more opportunities for detailed follow-up studies of the FRB. While we do not yet know whether repeaters and one-off FRBs are two separate classes (e.g., Z. Pleunis et al. 2021), the existence of repeaters demonstrates that the progenitors of at least some FRBs are not cataclysmic (L. G. Spitler et al. 2016; for a review of FRB models, see E. Platts et al. 2019).

Despite multiwavelength search efforts (I. Andreoni et al. 2020; C. D. Kilpatrick et al. 2021; C. Nunez et al. 2021; Z. Yan et al. 2024), no prompt counterparts to FRBs have been found.[26] However, long-lived counterparts have been seen in radio emission at frequencies between 100 and 22 GHz. In particular, two well-localized repeating FRBs, FRB 20121102A (S. Chatterjee et al. 2017) and FRB 20190520B (C. H. Niu et al. 2022), have each been associated with a long-lived "persistent radio source" (PRS). The PRSs that are coincident with FRB 20121102A and FRB 20190520B are similar: both are compact on milliarcsecond (mas) scales (B. Marcote et al. 2017; S. Bhandari et al. 2023b), have nonthermal (negative) spectral indices at a brightness temperature of $T > 5 \times 10^7$ K for FRB 20121102A, luminosities of $L_{\rm radio} \approx 10^{29}$ erg s^{-1} Hz^{-1}, and are spatially offset from the nuclei of their dwarf host galaxies by <10 pc. Both FRBs associated with these PRSs exhibit high and highly variable Faraday rotation measures (RMs; D. Michilli et al. 2018; C. H. Niu et al. 2022) suggesting a highly magnetized origin (e.g., B. Margalit & B. D. Metzger 2018).

PRSs are thus defined as long-lived compact radio sources that are brighter than the local star formation in the galaxy and are clearly not active galactic nuclei (AGN). It has been proposed that the luminosity of a PRS is correlated with the RM of the FRB if the RM primarily arises from the persistent emission region (Y.-P. Yang et al. 2020). Recently, a potential PRS with a positive spectral index ($\alpha \sim 0.97 \pm 0.54$) was reported for FRB 20201124A (G. Bruni et al. 2024). While the PRS luminosity correlates with the FRB's RM, similar to the other two confirmed PRSs, its lower luminosity, and other characteristics suggest a possible origin from star formation on a subarcsecond scale (K. Nimmo et al. 2022; Y. Dong et al. 2024a). The two confirmed PRSs have radio flux densities higher than that expected by star formation activities in their host galaxies. Their fluxes have also been observed to be variable over short timescales ($\lesssim$1 yr; e.g., L. Rhodes et al. 2023; X. Zhang et al. 2023). However, the time variability observed for the PRS of FRB 20121102A has been suggested to be a result of refractive scintillation as opposed to intrinsic (G. Chen et al. 2023).

It is possible that a single central engine could both produce FRBs and power the PRS. This general idea has been detailed in multiple models: the magnetar model (A. M. Beloborodov 2017; B. Margalit & B. D. Metzger 2018; B. Margalit et al. 2019; S. Bhandari et al. 2023b), gamma-ray burst (GRB) afterglows (K. Murase et al. 2016; A. M. Beloborodov 2017; B. D. Metzger et al. 2017), ultraluminous X-ray binaries (N. Sridhar et al. 2021; N. Sridhar & B. D. Metzger 2022; N. Sridhar et al. 2024), and synchrotron heating (Y.-P. Yang et al. 2016; Q.-C. Li et al. 2020), among others (E. Platts et al. 2019).[27] The PRS of FRB 20121102A exhibits analogous characteristics to the radio emission observed from a previous luminous supernova (SLSN; T. Eftekhari et al. 2019). This indicates a possible connection between the two classes of transients, with the SLSN being one of the proposed FRB progenitor channels. It is also possible for a PRS to be produced by the massive accreting black hole of the host galaxy (B. Zhang 2020).

If all repeating FRBs are associated with PRSs, this would have implications for their progenitor channels and emission mechanisms. In contrast, robust nondetections of PRSs in a sample of FRB repeaters (as recorded by, e.g., B. Marcote et al. 2020; F. Kirsten et al. 2022; K. Nimmo et al. 2022) could imply (i) a different progenitor channel for some events, (ii) that the physical conditions implied by the PRS in FRB 20121102A are not *required* for the production of repeating FRBs, or (iii) that PRSs have shorter lifetimes such that the emission is no longer detectable at the time of observations. It is also possible that PRSs could be associated with some one-off FRBs and not only with repeaters (C. J. Law et al. 2022). However, given that the two FRBs with PRSs and the one with a candidate PRS are all repeaters, these have shown that at a minimum PRSs are an important phenomenon associated with repeating FRB nature. While the first two discovery PRSs are remarkably similar, if confirmed, including FRB 20201124A brings diversity to the properties of the PRS population. This diversity inspires the need to identify and study more PRSs to understand their connection with FRBs and shed light on the emission mechanisms, progenitor channels, and population variation of FRBs (D. Vohl et al. 2023; Y. Dong et al. 2024b).

Typically, robust multiwavelength associations require $\lesssim 1''$ localizations for FRBs, and hence the detection of a burst with an interferometer (T. Eftekhari & E. Berger 2017; T. Eftekhari et al. 2018). However, T. Eftekhari et al. (2018) demonstrate that, due to the lower density of radio sources in the sky compared to faint optical sources (S. P. Driver et al. 2016b; Y. A. Gordon et al. 2021), robust FRB-PRS associations can be made for coarser localizations ($\sim 20''$). In addition, they argue that, for larger localization regions that preclude firm associations, constraints can still be placed on possible radio associations as a function of luminosity.

Arcsecond localizations are not available for most FRBs discovered by the Canadian Hydrogen Intensity Mapping Experiment (CHIME) telescope. Localizations with CHIME's best-recorded precision ($\sim 1'$) can be obtained using the channelized raw voltages of the FRB signals from the telescope feeds (i.e., the baseband data) following the techniques described by D. Michilli et al. (2021).

Although these baseband positions exceed the threshold of $\lesssim 20''$ found by T. Eftekhari et al. (2018) to robustly associate a radio source with an FRB based on probability of chance alignment arguments, it is still possible to search for radio sources within the CHIME/FRB localization regions. One can then analyze the properties of these radio sources along with their host galaxies to identify any that may originate from a source other than star formation or an AGN in their host galaxy. While follow-up observations would be necessary to

[26] The FRB-like burst of Galactic magnetar SGR 1935+2154 did show a hard X-ray burst counterpart (C. D. Bochenek et al. 2020; CHIME/FRB Collaboration et al. 2020).

[27] https://frbtheorycat.org/index.php/Main_Page

Table 1
Summary of Archival Radio Surveys Employed in This Study

Survey	Telescope	Observation Dates	Frequency (GHz)	Angular Resolution (arcsec)	Sky (deg^2)	Sensitivity Coverage[a] (mJy $beam^{-1}$)	N_r[b]	μ[c]	References
VLASS	VLA	2017−2024	2−4	2.5	33,885	0.12	3	3.9 ± 2.5	D. McConnell et al. (2020)
FIRST	VLA	1993−2004	1.5	5	10,575	0.15	2	3.9 ± 2.5	R. H. Becker et al. (1995)
NVSS	VLA	1993−1996	1.4	45	23,264	2.50	4	5.1 ± 2.7	J. J. Condon et al. (1998)
RACS	ASKAP	2019−2020	0.887−1.655	15	36,656	0.25	1	2.4 ± 2.1	D. McConnell et al. (2020)
TGSS ADR1	GMRT	2010−2012	0.150	25	36,900	3.50	2	0.7 ± 1.4	H. T. Intema et al. (2017)
LoTSS	LOFAR	2014−2021	0.10−0.24	6	5635	0.08	8	34.6 ± 6.4	T. W. Shimwell et al. (2022)

Notes.
[a] 1σ rms sensitivity.
[b] N_r is the number of radio sources found for each catalog in the FRB localization regions. Compared to μ, no catalog shows any excess radio source in the field (see Section 5.3 for a discussion).
[c] μ is the expected number of radio sources given the total area of CHIME/FRB fields searched that overlaps with each of these catalogs. The errors are propagated using N. Gehrels (1986) Poisson probability error function for 1σ values (see Section 2.5 for details).

confirm an FRB association with any radio sources of interest, such studies still have the potential to provide insights into the possible prevalence of PRSs or the depth of any nondetections.

This type of study serves as a precursor for classifying radio sources as PRSs for upcoming telescopes like the CHIME/FRB Outrigger project (C. Leung et al. 2021; T. Cassanelli et al. 2022; J. Mena-Parra et al. 2022; A. E. Lanman et al. 2024), the fast radio transient-detection program at MeerKAT (MeerTRAP; K. M. Rajwade et al. 2022), the Deep Synoptic Array (DSA-110; V. Ravi et al. 2023), and the Bustling Universe Radio Survey Telescope in Taiwan (H.-H. Lin et al. 2022), which will improve the number of precisely localized FRBs and allow for more robust multiwavelength association. Meanwhile, by leveraging a substantial sample of repeating FRBs discovered by CHIME/FRB, significant constraints can be placed on the presence of FRB 20121102A-like PRSs using CHIME/FRB repeaters and arcsecond radio continuum surveys.

In this work, we searched for and studied radio sources found within the localization regions of the 37 recently published CHIME/FRB repeaters for which ∼arcminute baseband localizations were available (M. Bhardwaj et al. 2021a, 2021b; D. Michilli et al. 2023; CHIME/FRB Collaboration & B. C. Andersen 2023). We report the data used for the search, relevant observations carried out, and the result of the search in Section 2. We then describe the multiwavelength data used and the diagnostic analysis carried out for each of the radio sources in Section 3 and Section 4 respectively. The summary of the search result and candidate potential PRSs are presented in Section 5. We then describe the implication of the radio sources in the context of existing FRB-PRS models in Section 6, followed by the conclusion in Section 7. Detailed results of individual radio sources can be found in Appendix A. In all cases, we convert redshifts to luminosity distances assuming a flat $\Lambda_{\rm CDM}$ cosmology with $H_0 = 67.7\ {\rm km\,s^{-1}\,Mpc^{-1}}$, $\Omega_{\rm m} = 0.31$, and $\Omega_{\wedge} = 0.68$ (Planck Collaboration et al. 2020).

2. A Search for PRS Candidates in the Localization Region of CHIME/FRB Repeaters

Here, we describe the process used to search for radio sources in the fields of CHIME/FRB repeaters. Specifically, after describing the FRB fields searched in Section 2.1, we describe the radio catalogs (Section 2.2.1) and targeted Very Large Array (VLA) observation images searched (Sections 2.2.2 and 2.2.3) and present the initial result of the searches (Sections 2.3 and 2.4). The probability statistics of the archival and deep VLA results are described in Sections 2.5 and 2.6.

2.1. FRB Sample

Of the 52 repeating FRBs presented by D. Michilli et al. (2023) and CHIME/FRB Collaboration & B. C. Andersen (2023), which represents almost all known repeaters, we have selected objects that have $\lesssim 2'$ localizations. This resulted in 37 FRB regions searched for PRSs including FRB 20181030A, and FRB 20200120E, which were initially presented by Bhardwaj et al. (2021a; 2021b). While for a majority of these FRBs, the baseband localization region is on order $1'-2'$; from the CHIME baseband positions, we note that two FRBs in our sample (FRB 20180916B; B. Marcote et al. 2020; and FRB 20200120E; F. Kirsten et al. 2020) have milliarcsecond positions available.

2.2. Radio Data

2.2.1. Radio Survey Catalog Search

We first searched for the presence of candidate PRSs within the 90% confidence level error regions of the 37 FRBs using archival radio catalogs from the VLA Sky Survey (VLASS; M. Lacy et al. 2020), the NRAO VLA Sky Survey (NVSS; J. J. Condon et al. 1998), the Faint Images of the Radio Sky at Twenty-Centimeters (FIRST; R. H. Becker et al. 1995) survey, the TIFR-Giant Metrewave Radio Telescope (GMRT) Sky Survey (TGSS; H. T. Intema et al. 2017), the Rapid ASKAP Continuum Survey (RACS; D. McConnell et al. 2020), and the high-resolution component of the LOw-Frequency ARray LOFAR Two-meter Sky Survey (LoTSS; T. W. Shimwell et al. 2022). For each survey, we list their frequency, angular resolution, sky coverage, and sensitivity in Table 1.

2.2.2. Deep VLA Observation

In addition, we have carried out observations of FRB repeater fields with the Karl G. Jansky VLA interferometer in different array configurations of the VLA, all in the $1-2$ GHz band, through program numbers 18B-405 (PI: Casey Law), 19B-223, 19A-331, 20B-280, 20A-469, 21B-176, and 21A-387 (PI: Shriharsh Tendulkar). In the $1-2$ GHz band, the full width at half power of the primary beam is $28'$, which is 14 times larger than the typical CHIME FRB localization region. Details of the observations are given in Table 2. No FRBs were detected in the commensal realfast (C. J. Law et al. 2018) observations during these programs.

The Common Astronomy Software Applications (CASA) package (J. P. McMullin et al. 2007) was used to perform the data reduction, flux measurement calibration, and imaging of the data. Specifically, we used the Python-based CASA pipeline tool `pwkit` released by P. K. G. Williams et al. (2017). We flagged for radio frequency interference (RFI) using the automatic AOFlagger (A. R. Offringa et al. 2010). The bandpass and phase calibration were carried out using the specified calibrators as listed in Table 2. After data reduction, we imaged the total intensity component (Stokes I) of the source visibilities, setting the cell size, so there would be $4-5$ pixels across the width of the beam. All calibrated data were imaged using the CLEAN algorithm, and primary beam correction was carried out. For cases where there is more than one observation of a particular field, we combine the calibrated visibilities in the UV-plane to produce a single higher-sensitivity image shown in Figure 1. There are some observations taken during the time when the VLA telescopes are moving from A to D configuration. We note that, as a result of this movement, the data quality from this setup could be poor and could affect the final image.

`AEGEAN` (P. J. Hancock et al. 2012, 2018) was used to find sources and measure fluxes and associated uncertainties within each image. The summary of all measured radio flux densities and upper limits are presented in Appendix Table 7, and discussed in Section 2.4 below.

Table 2
Summary of Deep Radio Observations with VLA at 1.5 GHz for Listed FRB Fields

FRB	Configuration	Date	Bandpass Calibrator	Phase Calibrator	rms Sensitivity[a] (μJy beam^{-1})	Ns[b]	Integration Time[c] (hr)
FRB 20180814A	B	2019 Mar, Jun, Jul	0542 + 498 = 3C147	J0410+7656	6.5	2	16
	A, A → D[f]	2020 Oct 22, 2021 Feb−Mar	0542 + 498 = 3C147	J0410+7656	5.4	4	11.5
	combined	combined	0542 + 498 = 3C147	J0410+7656	3.5	5	27.5[d]
FRB 20180916B	B	2019 June 7−22	0542 + 498 = 3C147	J0217+7349	6	0	12
FRB 20181030A	A → D[f]	2021 March 2−12	1331 + 305 = 3C286	J1035+5628	10	1	4
FRB 20190117A	BnA	2020 Nov 2	0137 + 331 = 3C48	J2139+1423	16	1	1
FRB 20190208A	A	2021 Feb 5−7	0137 + 331 = 3C48	J1852+4855	5	1	10
FRB 20190303A[e]	B, A → D[f]	2019 Nov, Dec, 2020 Jan	1331 + 305 = 3C286	J1313+5458	5	2	10
	A	2021 Feb	1331 + 305 = 3C286	J1352+3126	5	2	15.5
FRB 20190417A	A	2021 Feb 25−27	1331 + 305 = 3C286	J1944+5448	8.5	2	4
FRB 20200120E	A	2020 29 Dec, 2021 Jan 13−18	0542 + 498 = 3C147	J1048+7143	9	0	5

Notes. The results are from combined observations for all fields except for FRB 20190117A, which has a single observation.
[a] 1σ rms error of the image.
[b] Number of sources (Ns) within the FRB error region.
[c] The total on-source time including integration and overhead.
[d] Noise level obtained from the combination of the visibilities of all images from 2019, 2020, and 2021 in all arrays to enhance image resolution.
[e] Images were combined separately as shown in this table because of the morphology of the extended sources found in this field.
[f] A → D configuration is an observational setup at the time when the VLA telescopes are moving from A to D configuration. As a result of this movement, the data quality from this setup can be poor most of the time; hence, we advise caution when interpreting results from such setups.

2.2.3. Commensal VLITE Observations

Finally, we obtained simultaneous data for our VLA observations using the VLA Low-band Ionosphere and Transient Experiment (VLITE), which is a commensal low-frequency system on the VLA that operates in parallel with nearly all observing programs above 1 GHz (T. E. Clarke et al. 2016). VLITE records a parallel data stream during regular programs on a subset of up to 18 VLA antennas with a bandwidth of 64 MHz centered at 352 MHz. The VLITE data are correlated with a custom DiFX-based correlator (A. T. Deller et al. 2007) and processed through a dedicated calibration and imaging pipeline. The pipeline uses a combination of Obit (W. D. Cotton 2008) and AIPS (E. W. Greisen 2003) for standard reductions including removing RFI solving for the delay, complex gain, and bandpass. VLITE uses the R. A. Perley & B. J. Butler (2017) flux density scale, and an additional calibration uncertainty of 15% has been added to the measurement errors.

We used PyBDSF (N. Mohan & D. Rafferty 2015) to measure fluxes and associated measurement errors from the VLITE images. We present the measurements in Appendix Table 7 where nondetections within the error region are reported as 5σ upper limits.

2.3. Archival Search Result

Out of 37 FRB fields searched, 13 unique radio sources in the archival surveys were found in all the regions combined. Specifically, there are eight LoTSS radio sources within the localization regions for seven CHIME/FRB repeaters, four sources in NVSS, two in FIRST, two in TGSS, one in RACS, and three in VLASS.

Some of these radio sources are from the same location but seen at different epochs and frequencies as represented by the catalogs. In addition, we obtained upper limits on the flux densities for the potential existence of radio sources at the positions of the remaining 34 FRBs where there were no VLASS sources even though they are within the VLASS coverage. We adopt VLASS for this purpose, as it was the most sensitive catalog searched at GHz frequencies. A comprehensive investigation of the properties of these sources is presented in Section 4, and their flux density limits and frequencies are reported in Appendix Table 7.

2.4. Deep VLA Results

Here, we report the sources found in the field of the FRBs observed in deep VLA observations. Out of eight FRB fields imaged with deep-targeted VLA observations, there are six fields with one or more radio sources within the CHIME baseband error region. Specifically, we found five sources for FRB 20180814A, one source for FRB 20181030A, one source for FRB 20190208A, one source for FRB 20190117A, two sources for FRB 20190417A, and two sources for FRB 20190303A for a total of 12 radio sources from the deep VLA images. In Figure 1, we show the deep VLA images for these six fields with both the location of detected radio sources and the CHIME baseband localization region indicated. In addition, we compute the 5σ upper limit based on the rms noise within the localization region of the FRB in the final image. These would represent limits on the presence of a PRS in the event that none of the radio sources identified are associated with the FRB.

The other two FRBs (FRB 20180916B and FRB 20200120E) have subarcsecond positions from Very Long Baseline Interferometry (VLBI) that were used for the search instead. There is no radio source in the VLA images at the location of either FRB; hence, we measure 3σ flux density upper limits at these locations. In Figure 2, we show the radio nondetection in the deep VLA images for these two fields with the subarcsecond location of their FRBs indicated. A summary of measured radio flux densities and limits is given in Appendix Table 7.

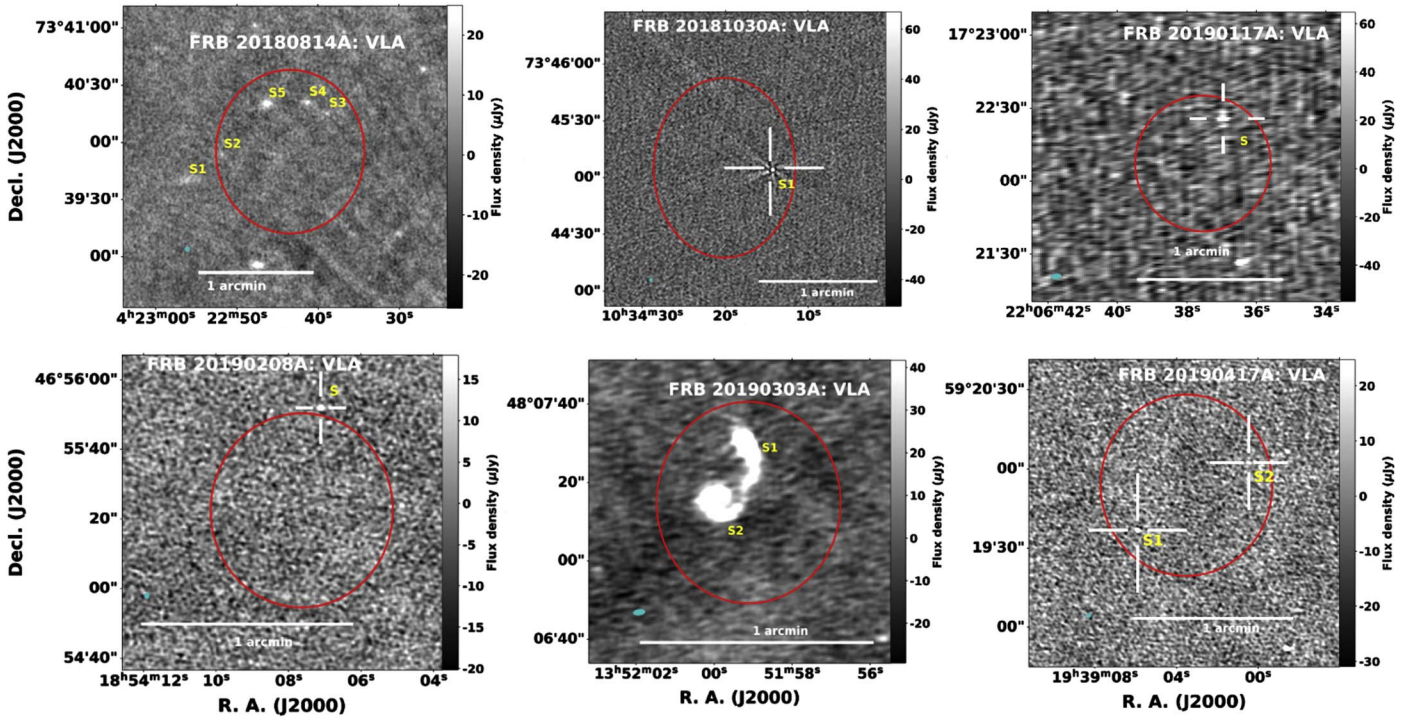

Figure 1. VLA images capturing the six FRB fields featuring detected radio sources (unresolved, resolved, and extended). The 90% confidence level baseband error regions of the FRBs are depicted as red ellipses. For some fields, the white crosshair marks the location of the sources, while others have the sources labeled with "*S*" corresponding to the number of radio sources in the field. The beam of each image is represented by a small cyan-colored ellipse at the lower left corner of each image.

2.5. Expected Number of Radio Sources, μ

While we will perform a detailed analysis to assess the potential origin of each radio source below, we can also compare the number of radio sources identified within the CHIME localization regions to expectations based on the source counts in each catalog searched. Doing so will allow us to assess whether there is any evidence for a (statistical) excess of sources compared to background levels, potentially due to association with the FRBs.

To do this, we used the total number of sources found for each catalog, the total sky area covered by the entire survey, and the total CHIME/FRB area that overlaps with the catalog to estimate the average number of sources (μ) expected from searching the entire CHIME/FRB region.[28] This value could be used to obtain the probability of finding the observed number of radio sources for each catalog. The errors on the expectation number are propagated using N. Gehrels (1986) Poisson probability error function for 1σ values. This analysis was done for all the catalogs searched, and the results are presented in Table 1. All catalog results have fewer or an equal number of sources compared to the expected number. Thus, we do not find evidence of an excess of sources in the CHIME localization regions at the depths covered by these archival surveys. While in most surveys the number of sources found is consistent within errors to the expected number, we note that the number of LoTSS sources identified is a factor of ∼4 lower than expected. This may mean that the ∼0.043 deg^2 covered by the CHIME repeater baseband regions searched in this study are not representative of the general source density found in the 5600 deg^2 covered by LoTSS DR2 (T. W. Shimwell et al. 2022).

2.6. Individual Chance Coincidence Probability, $P_{cc,rad}$, of Associating Each Radio Source to Its FRB

In addition to searching for statistical excesses of sources, we can also estimate the probability of chance coincidence between each radio source and its CHIME FRB localization region, $P_{\rm cc,rad}$, based on the size of the FRB uncertainty region and the flux density of radio source following T. Eftekhari et al. (2018; see Table 3 for a brief description). We assumed a Poisson distribution of radio sources across the sky by calculating the chance coincidence probability as $P_{\rm cc,rad} = 1 - \exp(-\pi R_{\rm FRB}^2 n(>S_\nu))$, where $R_{\rm FRB}$ is the 90% error radius of the FRB, S_ν is the flux density of the radio source, and $n(>S_\nu)$ is the number density of radio sources as bright or brighter than the flux density ($>S_\nu$) of the radio source found. For sources that were found from the deep VLA images and other archival sources at 1.4 and 1.5 GHz, we used the MeerKAT DEEP2 (A. M. Matthews et al. 2021) source count data set. For VLASS sources, we used the VLASS source count described by Y. A. Gordon et al. (2021), and for the other low-frequency radio sources, we assumed a spectral index of −0.71 according to Y. A. Gordon et al. (2021) to estimate their 1.4 GHz MeerKAT equivalent.

Given the size of the CHIME/FRB uncertainty region, we expect that the chance probability of associating the radio sources to the FRB ($P_{\rm cc,rad}$) will not be low; however, for completeness's sake, we report these values for the sources in Appendix Table 7. To accommodate effects resulting from multiple fields being searched, we also computed the adjusted chance coincidences following the application of the Bonferroni correction, also known as the "look-else-where" effect

[28] The expected number of radio sources, μ, is estimated as $\mu = \frac{A_{\rm b}}{A_{\rm cat}} \times N$, where N is the total number of sources from each catalog, $A_{\rm cat}$ is the area covered by a specific survey catalog, and $A_{\rm b}$ is the total area of the 90% confidence level of CHIME/FRB baseband regions searched.

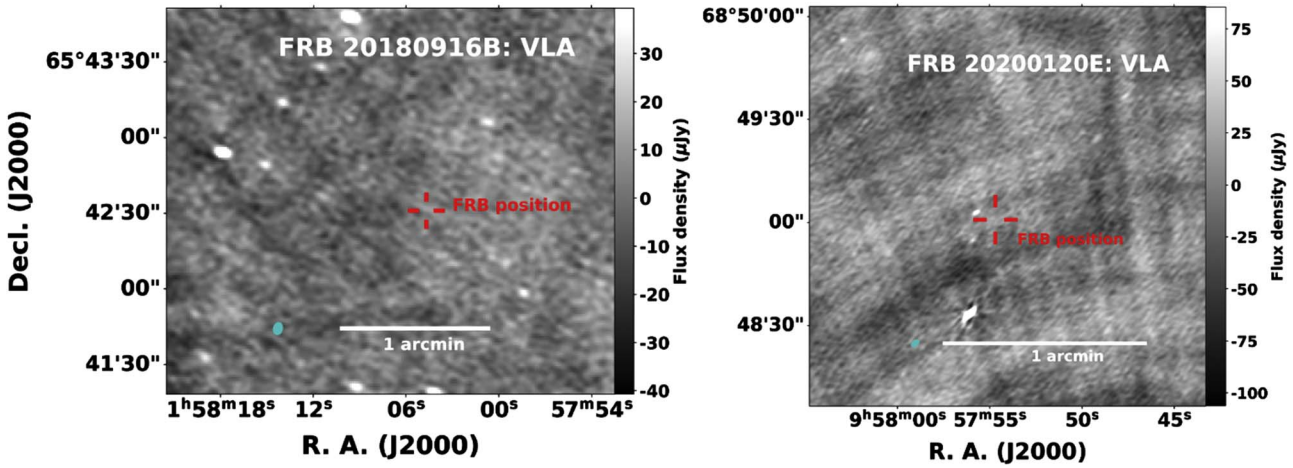

Figure 2. VLA images—FRB 20180916B and FRB 20200120E. There is no radio source at the location of these FRBs. The red crosshairs indicate the subarcsecond position of the FRBs but are much larger than the representative of the positional uncertainties.

(J. J. Goeman & A. Solari 2014). Consistent with the findings of T. Eftekhari et al. (2018), we find that, for localization regions of the size provided by CHIME baseband data, it is not typically possible to associate an individual radio source to a CHIME FRB based on purely statistical arguments. Finally, due to the difficulty with the accurate determination of flux densities of blended sources, we did not estimate $P_{\rm cc,rad}$ values for any such sources.

3. Multiwavelength Data for PRS Candidates

In total, we identified 25 radio sources within the CHIME localization regions of 37 repeating FRBs from both archival and targeted observations. As shown in Sections 2.5 and 2.6, in many cases, the ∼arcminute size of these localization regions precludes making a robust association with the FRB from statistical arguments. We will therefore rely on multiwavelength analysis to investigate the possible origin of each radio source and identify sources of particular interest as PRS candidates. Here, we describe the multiwavelength data that will be used in this analysis.

3.1. Optical and Infrared Photometry

3.1.1. Crossmatch with Optical Catalogs

We first searched for optical counterparts to the radio sources within 2″ of each radio source position using the Sloan Digital Sky Survey (SDSS; C. P. Ahn et al. 2012), The Pan-STARRS catalog (PS1; K. C. Chambers et al. 2016), and Dark Energy Spectroscopy Instrument (DESI), and Data Release 9 (DR9; A. Dey et al. 2019) Legacy Imaging Survey photometric catalogs. We use PanSTARRS/DESI catalog flags to verify that none of these optical sources are classified as probable stars. Out of 25 radio sources (including those found in archival surveys and the targeted VLA observations), we found optical sources that are spatially consistent with 17 of them. In Table 4, we list relevant properties of these optical sources that are provided by optical catalogs and will be used in the analysis in the following sections. This includes position, apparent r-band magnitudes, and half-light radius.

We did have a unique case of 20181030A-S where the radio source physically overlaps a spiral arm of the nearby ($D_L \sim$ 20 Mpc; G. Theureau et al. 2007) galaxy, NGC 3252. While the radio source is located ∼1′ from the galaxy nucleus, by visual inspection and considering the physical size of the galaxy, we infer that the radio source may be associated with the galaxy.

3.1.2. Gemini Photometry

In addition, as part of ongoing CHIME/FRB follow-up efforts, we requested deep Gemini imaging of the field of FRB 20190417A. The original motivation was the high dispersion measure (DM) of the FRB ($1378.2 \pm 2\,{\rm pc\,cm^{-3}}$; E. Fonseca et al. 2020). Given that higher DM can correspond to higher redshifts (J.-P. Macquart et al. 2020), this would allow us to search for fainter optical sources than previously identified by other surveys such as PanSTARRS and DESI.

Gemini North imaging of the field of FRB 20190417A was carried out in the r, i, and z bands on 2022 July 29th (for r band) and 2022 September 19th (for i and z bands). Total exposure time was 6×250 s for the i and r bands and 10×150 s for z band. The data were reduced using the standard packages of `gmos` and `gemini` routine in `PYRAF` (Science Software Branch at STScI 2012). This included overscan correction, flat-fielding, image alignment, mosaicing, and combination. The different exposure images were combined to produce a single image.

We used `PHOTUTILS` (L. Bradley et al. 2023) and `SExtractor` (E. Bertin & S. Arnouts 1996) source-finding software to carry out background subtraction and estimate the properties of the source associated with the radio source. Specifically, we measured the apparent magnitude by calibrating it against standard stars from PanSTARRS and then used the `iraf` routine to estimate the full width at half-maximum of the optical source to measure the half-light radius.

3.1.3. Infrared Photometry

For radio sources within the coverage, we retrieved photometric data for each of the radio sources from the Wide-field Infrared Survey Explorer (WISE; E. L. Wright et al. 2010) where available.

3.2. Optical Spectroscopy

For radio sources where we find an optical counterpart, we compile their spectroscopic redshifts and emission line fluxes when possible. These will be to estimate other galaxy properties in the sections below.

Table 3
Description of Probabilities and Expectation Values Used

Symbol	Name	Description	Sections	Tables
μ	Expected number of radio sources	Probability of finding the observed number of radio sources within the entire CHIME/FRB regions searched for each catalog	Section 2.5	Table 1
$P_{\rm cc,rad}$	Chance probability of association between a radio source and its FRB	Chance probability that a radio source is found within its FRB's uncertainty region	Section 2.6, A	Table 7
$P_{\rm cc,gal}$	Chance probability of association between a radio source and its host galaxy	Chance coincidence probability of associating a radio source to its plausible host galaxy. The value corrected for the Bonferroni effect is named $P_{\rm cc,RG}$	Section 4.5, A	Table 4

3.2.1. Archival/Published Spectroscopy

Redshift information was taken from the literature for some radio sources where the spectrum of their host galaxy is already published. Specifically, this was available for 20190303A-S1, 20190303A-S2, 20180814A-S (D. Michilli et al. 2023), as well as 20200223B-S and 20191106C-S (A. L. Ibik et al. 2024). Redshift information for these sources is listed in Appendix Table 8.

3.2.2. Gemini North Spectroscopy

In addition, we obtained observations of the likely host galaxies of 20190110C-S, 20190117A-S, and 20190417A-S1 with the Gemini Multi-Object Spectrograph (GMOS; I. M. Hook et al. 2004). The data were obtained on 2022 August 20 and 2022 September 20 for exposure times of (5×1200 s), (7×1200 s), and (6×1060 s) respectively. We used the $1\farcs0$ long-slit, R400 grating, and OG515 (>520 nm) blocking filter, at central wavelengths of 720/730 nm.

The data were reduced using the standard `gmos` and `gemini` packages in `PYRAF` (Science Software Branch at STScI 2012) and also with `PypeIt` (J. Prochaska et al. 2020). This included overscan correction, flat-fielding, sky subtraction, wavelength calibration, and extraction. The flux calibration was done using a standard star observed with the same setup on a different night. Chip gaps and cosmic rays were removed from individual exposures, and the different exposure spectra were combined to produce a final spectrum. All three GMOS spectra are shown in Figure 3.

For the spectrum of the plausible host galaxy of 20190117A-S (middle panel of Figure 3), there were no prominent emission or absorption features seen. We recorded the continuum-level flux caused by the emission. However, due to the lack of emission lines, we could not estimate the redshift of the galaxy.

For the spectrum of the plausible host galaxy of 20190110C-S (top panel of Figure 3), we found only one obvious spectroscopic emission feature located between 8000 and 8500 Å. (This feature was also visible in the 2D spectra.) If this feature corresponds to H_α, then the resulting redshift would be $z_{\rm spec} = 0.24$.

For the spectrum of the plausible host galaxy of 20190417A-S1 (bottom panel of Figure 3), we found late-type galaxy emission features. To estimate the redshift of the galaxy from the spectrum, we measured the observed central wavelengths of the H_α, H_β, [N II], and S II emission lines. We recorded a redshift of $z_{\rm spec} = 0.12817(2)$. The spectrum was then corrected to the rest frame and corrected for Milky Way extinction using the J. A. Cardelli et al. (1989) extinction law and an $E(B-V)_{\rm MW} = 0.0729$ mag from D. J. Schlegel et al. (1998). We find no evidence for significant additional internal extinction when calculating the Balmer decrement. The line fluxes of H_α, H_β, [O III] (λ5006 Å), and [N II] (λ6582 Å) were then measured by fitting a Gaussian profile to the rest-frame spectrum. The process was carried out in an automated manner and repeated 100 times to estimate the error in the line fluxes due to uncertainty at the continuum level.

4. Multiwavelength Analysis of PRS Candidates

Here, we present a detailed multiwavelength analysis of each of the radio sources identified in the CHIME/FRB localization regions. Our primary goal is to assess their potential nature with the aim of identifying promising PRS candidates. Throughout, we will use the properties of the previously published PRSs as shown in Table 5 as a guide, while also focusing on properties that can be used to assess whether the radio sources are simply consistent with expectations for either (i) star formation in their host galaxies or (ii) AGN.

4.1. Size of the Radio Source

The size of a radio source is a key property for deciding its nature. Based on the two confirmed examples to date (FRB 20121102A and FRB 20190520B), PRSs are expected to be compact (< 10 pc; B. Marcote et al. 2017; S. Bhandari et al. 2023b). Given the frequency of our observations and the typical beam size of the VLA, we, therefore, expect similar PRSs to be unresolved in our data, even for relatively nearby events.[29]

We therefore characterize the extent of each radio source using measurements of their semimajor axis, semiminor axis, and position angle. We classify sources into one of three categories: (i) unresolved, corresponding to sources where the ratio of the area of the radio source to the beam size is $\lesssim$1.2, (ii) resolved sources, which are radio sources whose size exceeds that of their beam and can be fit by a single 2D Gaussian, or (iii) extended sources, which we identify as sources that can be fit by more than one Gaussian component, including both multicomponent and complex sources. We adopt a threshold of $\lesssim$1.2 for our definition of unresolved sources because it can be difficult to define the edge of some sources with respect to that of the beam. The categories assigned to each detected radio source are listed in Appendix Table 7.

Of the 25 radio sources identified, 10 are unresolved by our definition. Moving forward, we only consider these as potential PRS candidates. These candidates include, specifically,

[29] For an example, at a redshift of $z_{\rm spec} = 0.1$, beam size of $1\farcs3$—representative for the VLA in A configuration and 1.5 GHz—would place a relatively conservative limit on the size of the radio-emitting source of <2.4 kpc.

Table 4
Radio-to-optical Association Results

Radio Source	Radio Catalog	R.A.$_{gal}$ (J2000)	Decl.$_{gal}$ (J2000)	z[h]	m_r (mag)	R_{50} (arcsec)	Optical Catalog	Offset (arcsec)	RO Ratio[g]	$P_{cc,gal}$[a]	$P_{cc,RG}$[a]
20181030A-S1	VLA	10:34:14.25	+73:45:53.9	0.00385	12.88	31.72[f]	(NGC 3252)	57.6 ± 0.1[c]	⋯	0.0015	0.0532
20190110C-S	VLASS	16:37:17.82	+41:26:34.1	<0.22	22.32	0.66[f]	SDSS/DESI	0.24 ± 0.07	2.3	0.0252	0.6106
20200619A-S	VLASS	18:10:17.35	+55:37:15.5	<0.45	20.40	0.68[e]	PS1/DESI	0.44 ± 0.13	1.9	0.0054	0.1803
20190208A-S	VLA	18:54:07.11	+46:55:51.9	<0.68	20.44	0.22[e]	PS1/DESI	0.04 ± 0.03	0.5	0.0005	0.0195
20190117A-S	VLA	22:06:36.96	+17:22:25.7	<0.46	23.48	0.1[b,e]	DESI	0.08 ± 0.07	2.2	0.0020	0.0705
20190417A-S1	VLA	19:39:05.82	+59:19:36.7	0.128	21.47[d]	0.3[d,e]	DESI/Gemini	0.56 ± 0.06[d]	1.3	0.0049	0.1659

Notes. This table displays exclusively unresolved radio sources linked with either extended/resolved or unresolved galaxies.
[a] $P_{cc,gal}$ is the chance coincidence probability of finding an optical source of the given magnitude and half-light radius while $P_{cc,RG}$ is the value corrected for "look-elsewhere-effect" (see Section 4.5 and Table 3).
[b] This source is classified by DESI to be a point source with a low probability of being a star; hence, there is no measurement of its half-light radius. Given the nature of the optical source, we adopted 0.″1 for the calculation of the chance coincidence calculation.
[c] The radio source is at the edge of a close by NGC galaxy, hence the reason for the large offset.
[d] The optical source information was obtained from Gemini photometry (see Section 3.1.2 for details).
[e] Unresolved optical counterpart.
[f] Extended optical counterpart.
[g] RO ratio is the logarithm of the radio-to-optical flux ratios according to RO ratio = $\log_{10}$ ($S_{1.4\ GHz}/F_{opt}$), where values <1.4 implies star formation-related radio emission (see Section 4.6).
[h] Redshifts' limits are the FRB z_{max} while the others are z_{spec} of the optical counterpart of the radio source. Details on the redshifts of the sources are presented in Appendix Table 8.

20200619A-S, 20190110C-S, 20181030A-S1, 20190208A-S, 20190117A-S, and 20190417A-S1, which have likely optical host associations, as well as 20180814A-S2, 20180814A-S3, 20181119A-S, and 20191114A-S, which lack a coincident optical association.

4.2. Redshift Cutoff and Luminosity

In order for a radio source to be a viable PRS candidate, it must not be located at a redshift higher than the maximum allowed for the FRB based on its DM. We take values of DM and z_{max} already published by CHIME/FRB Collaboration & B. C. Andersen (2023) and D. Michilli et al. (2023). For cases where they are not available, we calculate z_{max} using the `FRUITBAT` software (A. Batten 2019) by subtracting the DM contribution expected for the disk of the Milky Way from the NE2001 model (J. M. Cordes & T. J. W. Lazio 2002), DM_{MW}(NE2001), but do not attempt to correct for contributions from either the MW halo (DM_{halo}) or the FRB host galaxy (DM_{host}) to be conservative. In Appendix Table 8, we list z_{max} for all FRBs in our sample.

Of the 10 unresolved radio sources described above, we have spectroscopic redshifts for the underlying galaxies for three of them. Of these, the probable hosts of 20181030A-S1 and 20190417A-S1 have lower z_{spec} than the z_{max} for their respective FRBs, and thus remain viable. For 20190110C-S, the tentative redshift of $z_{spec} = 0.24$ (which was based on a single emission line) is slightly higher than the $z_{max} = 0.22$ of the FRB. However, because there is uncertainty in this redshift estimate, we chose to still consider this source in the analysis in the following sections. Of the remaining unresolved radio sources, four have no detected optical counterparts, and three others have no redshift information. As a result, we do not rule out any of the 10 unresolved sources as PRS candidates due to their redshifts.

In addition, for each radio source detected within the vicinity of each FRB, we utilize the z_{spec} of its host galaxy to compute the luminosity and other relevant properties of the radio source. In instances where a spectroscopic redshift is unavailable, we employ the z_{max} of the FRB, estimated from the DM, to derive an upper limit for the luminosity of the radio source. The observed spectral luminosities are listed in Appendix Table 8.

4.3. Variability and Spectral Shape

The current limited sample size makes it difficult to determine the time-dependent properties and spectral shapes of PRSs. While the two known PRSs exhibit short-term variability (<1 yr; S. Chatterjee et al. 2017; C. H. Niu et al. 2022), they also appear to vary at longer timescales (e.g., >1 yr for FRB 20121102A; L. Rhodes et al. 2023). However, the observed time variability seen for the PRS associated with FRB 20121102A (S. Chatterjee et al. 2017; B. Marcote et al. 2017) may be attributed to refractive scintillation rather than intrinsic source variability (G. Chen et al. 2023). The two known PRSs exhibit nonthermal spectral shapes, consistent with synchrotron emission (SE), with FRB 20121102A displaying a broken power-law spectral shape. However, we note that the PRS candidate FRB 20201124A shows a positive spectral index. Due to the significant uncertainty surrounding their variability and spectral characteristics, we refrain from using these traits to define PRSs. Instead, we present our observations to contribute to a better understanding of these sources as the sample size grows in the future. In this subsection, we investigate the variability and spectral indices of the identified radio sources.

For radio sources (among the 10 unresolved sources) with more than two detections at the same frequency but different times, we generate a light curve and calculate the variability of the source, V_s, using the $t-$ statistical methods outlined by K. P. Mooley et al. (2016) as $V_s = |\Delta S/\sigma_S| \geqslant 5$ where $\Delta S = S_2 - S_1$, and σ_S is the standard deviation between the two fluxes used. We adopt V_s

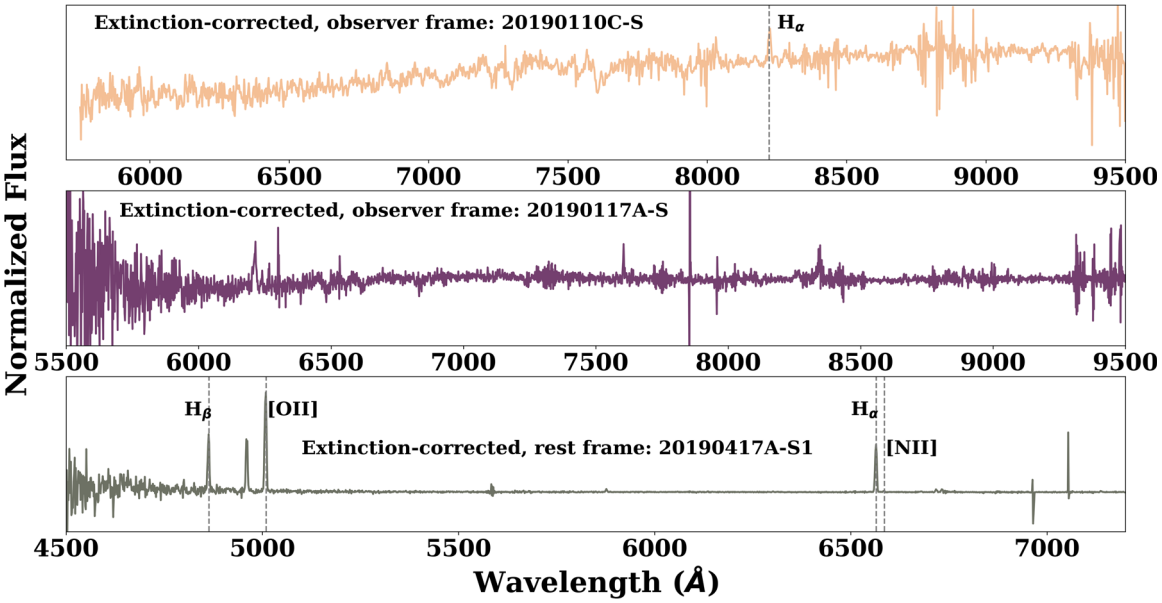

Figure 3. Gemini North spectra for the plausible host galaxies of radio sources 20190110C-S (top panel), 20190117A-S (middle panel), and 20190417A-S1 (bottom panel). In the top panel, the spectrum exhibits a bright emission line, possibly H_α, which is also clearly visible in the 2D spectra. In the middle panel, there are no prominent emission or absorption lines, making it unsuitable for estimating the redshift of the likely host galaxy of 20190117A-S. In the bottom panel, the spectrum of the likely host galaxy of 20190417A-S1 displays distinct emission line features, indicated by dashed gray lines. These lines were used to derive a redshift of $z_{\rm spec} = 0.12817(2)$ and other properties of the galaxy as discussed in Section A.9.

values >5 (at 5σ) as variable sources. Due to limited data availability, we are unable to make definitive statements regarding variability for most of the radio sources. Using VLASS epochs 1 and 2 for two radio sources, namely, 20200619A-S and 20190110C-S, we record V_s values of 0.35 and 0.36 respectively, indicating the absence of detected variability within a 2 yr timescale. However, we recorded $V_s = 16$ within 10 days of VLA observations at 1.5 GHz for 20181030A-S1, which could be due to refractive scintillation. This source is particularly interesting given its short-scale variability behavior, which is similar to that seen for the PRS of FRB 20121102 and FRB 20190520B at similar frequencies.

For the 10 unresolved radio sources, we estimate their spectral indices via multiple methods: (i) for the six sources identified in targeted VLA imaging, we use the first and second Taylor terms of the Stokes's images, I_0 and I_1, alongside their image residuals to estimate the in-band spectral indices and their uncertainties according to $\alpha = I_1/I_0$, (ii) for the six sources identified in targeted VLA imaging, we also use upper limits from contemporaneous VLITE observations to places limits on α, and (iii) for the four sources identified in archival surveys, we use detections in multiple surveys/frequencies to estimate the spectral indices. For methods (i) and (ii), the results are consistent with errors, except for one source (20190417A-S2). For method (iii), we caution that these observations were taken at different times (in some cases, more than 10 yr apart), and thus should be treated with caution. Results are listed in Appendix Table 8 and shown in Figure 4, where contemporaneous observations are connected by solid lines. All these radio sources seem to exhibit a nonthermal spectral shape except for 20181119A-S, which has a positive spectral shape similar to the spectral shape of the low luminosity PRS of FRB 20201124A ($\alpha \sim 0.9$) (G. Bruni et al. 2024). The nonthermal shape of the other radio sources is consistent with the spectral indices recorded for FRB 20121102A ($\alpha = -0.27 \pm 0.24$, B. Marcote et al. 2017) and FRB190820B ($\alpha = -0.41 \pm 0.04$, C. H. Niu et al. 2022).

4.4. Offset between Radio Source and Optical Sources

For the six radio sources that are both unresolved and have nearby optical associations, we calculate the offset between the radio and optical sources. These offsets will be used both to comment on the possibility that the radio source(s) may be due to AGN in their host galaxies and to calculate the probability of chance association between the radio and optical sources in Section 4.5 below.

In Table 4, we list the angular offsets with their associated uncertainties for all six radio sources. Also listed are the calculated half-light radii for each of the optical sources. In four cases, the optical sources are unresolved; while in two cases, they are resolved. In the latter case, host-galaxy normalized offsets can also be estimated. For the two sources with spectroscopic redshifts—20181030A-S1 and 20190417A-S1—the angular offsets correspond to physical offsets of 5.59 ± 0.01 kpc and 1.68 ± 0.18 kpc, respectively.

For one of the six radio sources (20181030A-S1), the high offset rules out an AGN in the underlying optical galaxy (although the possibility that it is a background source, unassociated with the optical galaxy, will be discussed below). The remaining five sources all have offsets from the underlying optical sources of $\lesssim 0\farcs5$. Given the uncertainties in these offsets, as well as the potential for some systematic offsets between the astrometry in radio and optical images, these sources may be consistent with the nuclei of their hosts. While AGNs are expected in the centers of galaxies, we note that it is still possible for a PRS to be found near the center of its host, similar to what was seen for the PRS of FRB 20121102A[30]

[30] The host galaxy of FRB 20121102A is a dwarf galaxy. As a result, the nucleus of the galaxy may not be well defined to clearly determine an accurate offset.

Table 5
Summary of the Properties of Known PRSs

PRS Property	FRB 20121102A[a]	FRB 20190520B[a]	FRB 20201124A[c]
Size (pc)	<0.7	<9	<700
z_{spec}	0.19273	0.24	0.098
ν (GHz)	1.6	1.7	15
L_ν (erg s^{-1} Hz^{-1})	2.8×10^{29}	3.0×10^{29}	5.3×10^{27}
Spectral index, α	-0.4 ± 0.5	-0.41 ± 0.04	1.00 ± 0.43
Offset	<12 mas (<40 pc)	20 mas (80 pc)	$0\farcs1$
DM (pc cm^{-3})	558.0	1204.7	413
RM (rad m^{-2})	1.46×10^5	2×10^5	−889.5

Notes.
[a] Details taken from S. Chatterjee et al. (2017), S. P. Tendulkar et al. (2017), and B. Marcote et al. (2017).
[b] Details taken from C. H. Niu et al. (2022) and S. Bhandari et al. (2023b).
[c] This is a candidate PRS, and information was taken from G. Bruni et al. (2024).

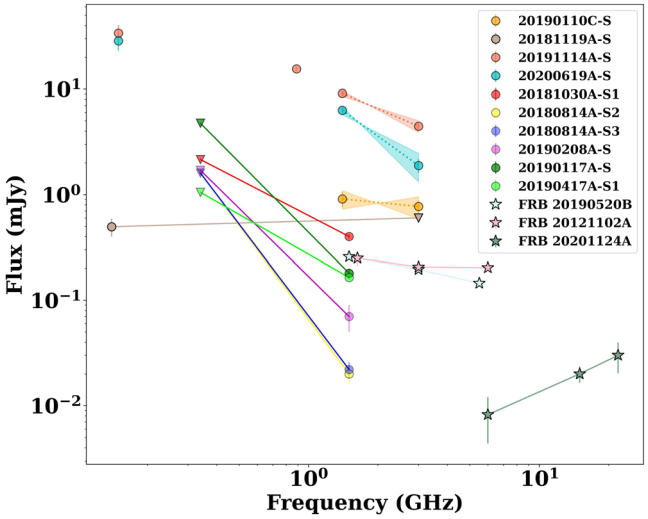

Figure 4. Spectral energy distribution of the unresolved radio sources shown as colored circles while the colored stars are known PRSs (FRB 20121102A, FRB 20190520B) and a potential third PRS. In general, most of the sources have nonpositive spectral shapes similar to that seen for FRB 20121102A and FRB 20190520B. 20181119A-S (brown) is the only source with a positive spectra shape among the radio sources but similar to that of the potential PRS of FRB 20201124A. Solid lines connect contemporaneous flux periods.

(offset = $0\farcs2$; S. P. Tendulkar et al. 2017). We therefore do not explicitly eliminate any PRS candidates based on this metric, but will consider this along with other properties below.

4.5. Chance Probability of Association between the Radio Source and Its Plausible Host Galaxy, $P_{cc,gal}$

As described above, 6 of the 10 unresolved radio sources identified in our search physically overlap with an optical source. In instances where we fail to identify optical counterparts, this may be attributed to limitations in the magnitude depth of the searched public archival catalogs, potentially rendering them unable to detect high-redshift sources, or it may be due to the absence of an optical counterpart for the radio sources themselves. However, even for cases where we identify potential optical counterparts, it is necessary to assess the chance coincidence probability, $P_{cc,gal}$ of associating the radio source to its optical counterpart that is a galaxy of a given brightness, m_r (see Table 3 for a quick description).

We assumed a Poisson distribution of galaxies across the sky and calculated the probability of a chance coincidence occurring within a radius, R using $P_{cc,gal} = 1 - \exp(-\pi R^2 \sigma(\leqslant m_r))$. The r-band galaxy number count reported by S. P. Driver et al. (2016a) was used to calculate the projected areal number density of galaxies brighter than the host-galaxy r-band magnitude, $\sigma(\leqslant m_r)$. To estimate R, we applied the prescription described by J. S. Bloom et al. (2002) given as $R = \max[2R_{radio}, \sqrt{R_0^2 + 4R_{hlg}^2}]$, where R_{radio} is the error radius of the radio source, R_0 is the offset between the radio source and its host galaxy, and R_{hlg} is the half-light radius of the host galaxy. The result of this calculation gives $P_{cc,gal}$ and is reported for each radio source with associated optical counterparts in Table 4.

While this formalism for the probability of chance alignment is common in the field of transients, we also computed adjusted chance coincidences using the Bonferroni correction—also known as the "look-elsewhere" effect. This accounts for the fact that we simultaneously searched 37 different CHIME/FRB localization regions for radio sources, and thus may expect to find even relatively low probability alignments with some frequency. This correction is represented by the equation $P_{cc,RG} = 1 - (1 - P_{cc,gal})^n$, where n is the number of fields examined ($n = 37$ in our case). These adjusted values are also listed in Table 4.

Examining Table 4, we see that five of the sources have $P_{cc,gal} \lesssim 0.005$, indicating a strong likelihood of association with their optical counterparts. The remaining source has $P_{cc,gal} \sim 0.025$. While the look-elsewhere effect naturally raises the possibility that we would identify an individual source with $P_{cc,gal} < 0.01$ (which corresponds to 1% probability) by chance (see the final column in Table 4), it is unlikely for all six sources to be so. We therefore proceed with analysis in the sections below that assume the optical and radio sources are associated.

4.6. Radio-to-optical Ratio

Given that some of our sources are close to the centers of their likely host galaxies based on their projected offsets, we need an additional diagnostic method to check whether the radio source is consistent with expectations for either star formation or AGN emission. Fortunately, the radio-to-optical flux ratio (RO ratio) of the source can provide just such a diagnostic metric.

We calculate the ratio as RO ratio = $\mathrm{Log}_{10}(S_{1.4GHz}/F_{opt})$ where $S_{1.4GHz}$ is the flux density in Jansky of the radio source at 1.4 GHz, and F_{opt} is the optical flux density in Jansky obtained

from the AB r-band magnitude of the galaxy according to the equation $F_{\rm opt} = 3631 \times 10^{-0.4 m_r}$ (e.g., J. Machalski & J. J. Condon 1999; J. Afonso et al. 2005; N. Seymour et al. 2008). Using this formalism, T. Eftekhari et al. (2021) adopt a rough threshold where RO ratio < 1.4 is consistent with star formation, and RO ratio >1.4 is consistent with AGN activities or other radio emissions such as pulsar wind nebula (PWN), hypernebula, supernova (SN) remnants, GRB afterglows, etc.

Using this same threshold, among the five unresolved radio sources with probable host-galaxy associations and offset $<1''$, we find that 20190208A-S (RO ratio $\sim$0.5) is likely due to star formation. When the RO ratios of the remaining four radio sources—20190110C-S ($\sim$2.3), 20200619A-S ($\sim$1.9), 20190117A-S ($\sim$2.2), and 20190417A-S1 ($\sim$1.3)—are compared with that of the PRS of FRB 20121102A (RO ratio = 2.9 using 250 μJy at 1.63 GHz) and FRB 20190520B (RO ratio = 1.7 using 258 μJy at 1.5 GHz), their RO ratios are consistent with either AGN or PRSs.

We note that we do not calculate an RO ratio for the sixth source that has a large offset but overlaps the spiral arm of a nearby galaxy (20181030A-S) because using the PanSTARRS template images we do not identify a specific optical counterpart at the location of the radio source.

4.7. Infrared WISE Diagnostic Analysis of the Radio Source

In order to further assess if there is any evidence for either AGN activity or obscured star formation in the galaxies associated with our PRS candidates, we examine their infrared colors from WISE (E. L. Wright et al. 2010). In the case where there is a WISE detection, we take the WISE band values from the archives and overplot the color ratios on the WISE diagnostic plot of E. L. Wright et al. (2010). The WISE diagnostic plot allows us to classify the infrared emission from our radio sources into different types of emission. From the plot, the parameter spaces overlapping with starburst, low-ionization nuclear emission-line regions' (LINERs') galaxies, ultra/luminous infrared galaxies, quasi-stellar objects, Seyferts, and obscured AGN are regarded as dusty regions (e.g., N. A. Reddy et al. 2006; E. L. Wright et al. 2010; N. Reddy et al. 2012; D. Stern et al. 2012; T. H. Jarrett et al. 2017).

Comparing the ratios, we conclude that one of our radio sources (20200619A-S) along with the PRS associated with FRB 20190520B has inferred colors consistent with star-forming galaxies without much dust contribution. 20190110C-S is consistent with an AGN, Seyfert, or dusty galaxies while 20190117A-S and the PRS of FRB 20201124A are consistent with a dusty star-forming environment. There is no detected WISE sources at the locations of 20190208A-S, 20181030A-S1, or 20190417A-S1 nor the PRS associated with FRB 20121102A.

4.8. Star Formation Rates

It is possible to further assess whether the detected radio sources are consistent with, or in excess of, expectations for star formation from their host galaxies by comparing the star formation rate (SFR) inferred from the radio flux to that from other metrics, such as H_α luminosity. Out of the six unresolved radio sources with host associations, only one (20190417A-S1) has H_α flux measurement required for this analysis. In particular, we note that, while we obtained spectra for both

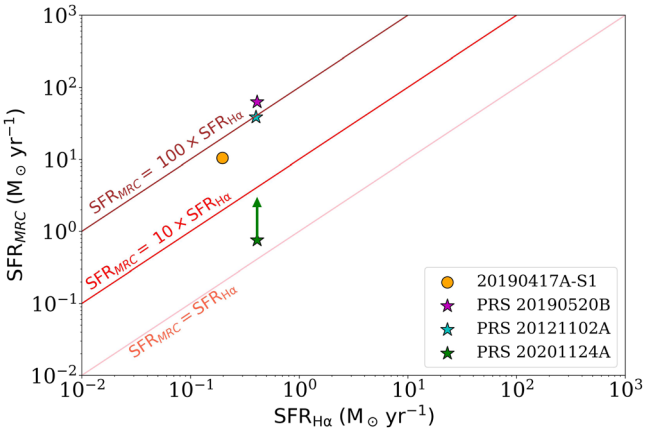

Figure 5. A plot of midradio continuum star formation rate, SFR_{MRC} vs. H_α estimated star formation rate in the context of that for FRB 20121102A (cyan), FRB 20190520B (magenta), and FRB 20201124A (dark green) with the SFR_{MRC} of the first two estimated from their 1.5 GHz PRS luminosity. The SFR_{MRC} plotted for FRB 20201124A is from the 6 GHz flux density and represents the lowest possible SFR_{MRC} as indicated by the gray upward arrow. The location of the orange circle (20190417A-S1) indicates that there is an additional cause of radio emission responsible for the observed emission.

20190117A-S and 20190110C-S, no emission lines were present in the former, and only one line was visible in the latter (leading to uncertainty in its identification). In addition, we have the global H_α flux available for the galaxy that overlaps with 20181030A-S1 (located in one of the spiral arms), but we do not have a measurement of H_α flux at the location of the radio source, as would be necessary to assess if it is consistent with an unresolved knot of star formation. While there is a tentative H_α detection for 20190110C-S, we do not consider it for this analysis because of the uncertainty in $z_{\rm spec}$.

To complete this assessment, we use the relationship of E. J. Murphy et al. (2011) to convert H_α luminosity to an SFR (SFR_{H_α}) and the equations from F. S. Tabatabaei et al. (2017) to assess implications for the radio SFR. The equations from F. S. Tabatabaei et al. (2017) include contributions to the radio flux from both thermal and nonthermal sources, and we use them to compute a midcontinuum radio-inferred SFR (SFR_{MRC}). For these calculations, we assume an electron temperature of 10^4 K, a nonthermal spectral index of $\alpha = -0.8$, and a ratio of thermal to total star formation of 0.1 at 1.5 GHz (see Table 6 of F. S. Tabatabaei et al. 2017). We use a Monte Carlo method to propagate the uncertainty in the radio flux density to SFR_{MRC}. We simulate 1000 flux density values, drawing from a Gaussian probability distribution with the same 1σ uncertainty as for the radio source. We then use these to calculate 1000 SFR_{MRC} values and record their mean and standard deviation.

Based on this analysis, the observed radio flux ($SFR_{MRC} = 10.41 \pm 0.53\ M_\odot\,{\rm yr}^{-1}$) of 20190417A-S1 is significantly higher than what would be expected based on the optical SFR ($SFR_{H_\alpha} = 0.20\ M_\odot\,{\rm yr}^{-1}$). This is evident in Figure 5 where we plot the SFR_{H_α} versus SFR_{MRC} showing either that a significant fraction of the star formation in the host of 20190417A-S1 is obscured or that another emission source is responsible for the radio emission. Unfortunately, no WISE color information is available for the host of 20190417A-S1. Also shown are the two previously reported PRSs and the potential PRS of FRB 20201124A. As can be seen, 20190417A-S1 (orange) falls in a similar location to both FRB 20121102A (cyan) and FRB 20190520B (magenta).

The $SFR_{H_\alpha} = 0.033\ M_\odot\ yr^{-1}$ that we have for 20181030A-S1 is not from the local neighborhood of the potential PRS; hence, we could not use it for this analysis. However, we calculate $SFR_{MRC} = 0.02\ M_\odot\ yr^{-1}$ for 20181030A-S1 and compare it with typical values of $SFR_{H_\alpha} \sim 10^{-4}\ M_\odot\ yr^{-1}$ for individual H II regions from P. A. Crowther (2013). SFR_{MRC} is over 100 times greater than SFR_{H_α} values for most H II regions indicating either that there is an extreme star-forming region in this exact location of NGC-3252 or that another emission source is responsible for the radio emission. The fact that SFR_{MRC} is greater than SFR_{H_α} for each of these sources suggests that there is additional radio emission beyond what can be attributed to unobscured star formation (which would be visible in H_α). This excess radio emission could, in principle, be due to multiple sources including (i) a PRS, (ii) an AGN, or (iii) obscured star formation. In Section 5.1, we will consider this information with other metrics described above (e.g., WISE IR diagnostics, optical-to-radio radio) to assess the most promising PRS candidates within our sample.

5. Summary of PRS Search and Candidates

Out of a sample of 37 CHIME/FRB fields searched, we identified a total of 25 radio sources: 13 archival sources (including an NVSS source near FRB 20181030A that has been reported by M. Bhardwaj et al. 2021b), and 12 radio sources from the deep VLA observations. In the Appendix, Tables 7 and 8 show the properties of all the radio sources. Out of 25 radio sources, there are 10 unresolved sources while the rest are resolved/extended sources.

In Section 5.1 below, we summarize the result of the multiwavelength analysis for the 10 unresolved radio sources and conclude which are the most promising PRS candidates. We then place deep limits on the presence of a PRS for all the FRBs observed with VLA in Section 5.2 and discuss the global implication for the radio search result in Section 5.3.

5.1. Summary of Potential PRS Candidates

Our ability to characterize each of the 10 unresolved radio sources identified varies based on the quantity of multi-wavelength data available, in particular likely optical host associations and redshifts. Here, we discuss individual radio sources, progressing with those from most to least information about their putative hosts.

Two of the unresolved radio sources have positions that overlap with optical galaxies for which we have secure redshifts that are lower than z_{max} for the FRBs. 20181030A-S1 overlaps with a spiral arm of the nearby NGC 3252 (which was identified by M. Bhardwaj et al. 2021b as the most probable host for this FRB), while 20190417A-S1 is offset $\sim 0\farcs5$ from an unresolved optical galaxy at $z_{spec} = 0.128$. Both sources show similarities to confirmed PRSs associated with FRB 20121102A and FRB 20190520B. Both have nonthermal spectral indices (Section 4.3) and, if associated with their underlying galaxies, have luminosities of 3.1×10^{35} and $1.1 \times 10^{38}\ erg\ s^{-1}$, respectively. The latter is similar to previously identified PRSs, while the former is multiple orders of magnitude less luminous.

In terms of other possible origins, both 20181030A-S1 and 20190417A-S1 have radio luminosities in excess of expectations for star formation within their hosts (local in the case of 20181030A-S1; Section 4.8). In both cases, we also disfavor that they are AGN in the underlying optical galaxy. For 20181030A-S1, this is due to its significant offset from the nucleus of NGC 3252. For 20190417A-S1, the optical spectrum obtained shows narrow emission lines with ratios indicative of a star-forming galaxy on a "Baldwin, Phillips & Terlevich" (BPT) diagram (see Appendix Section A.9). Its position is also offset from the galaxy center at $>3\sigma$, although we caution that this does not consider possible astrometric offsets between optical and radio images. While the radio sources could be background AGN, unassociated with the identified optical galaxies, we found a probability of chance alignment of $<0.05\%$ for both (Section 4.5). In the case of 20181030A-S1, this low probability is driven primarily by the rarity of $m_r \sim 13$ mag galaxies, although we note that background AGN have been identified in other nearby galaxies (e.g., P. Massey et al. 2019). While we do not identify a specific counterpart to the radio sources in archival optical, UV, or X-ray catalogs, we cannot formally rule out this possibility. However, despite this, we consider both 20181030A-S1 and 20190417A-S1 promising PRS candidates.

Four additional unresolved radio sources identified in our search have associated optical counterparts, all of which also have spectral indices consistent with nonthermal emission. For two of these sources, we obtained optical spectroscopy of the underlying optical sources (Section 3.2). The spectrum of the optical source underlying 20190110C-S showed a single emission line, which if interpreted as H_α places it above z_{max} for the FRB (Section 4.2). While this is tentative, most other reasonable interpretations for the line would place the source at even higher redshifts. In addition, the colors of the optical source are relatively red ($g - r$ color of ~ 4), and the WISE diagnostic colors overlap with AGN/Seyfert galaxies (Section 4.7). We therefore consider it unlikely to be a PRS. The radio source 20190117A-S has a position consistent with the centroid of its (unresolved) optical counterpart. However, an optical spectrum does not reveal any prominent emission lines indicative of AGN activity, and WISE infrared colors are more consistent with dusty galaxies. Thus, while the RO ratio is in excess of typical expectations for star formation (Section 4.6), future analysis examining the possibility of obscured star formation would be necessary to assess the viability of this source as a PRS.

For the final two sources with optical associations, we have not yet obtained any optical spectroscopy. 20190208A-S has a position consistent with the centroid of its (unresolved) optical counterpart. In addition, its RO ratio is consistent with expectations for star formation (Section 4.6). In contrast, 20200619A-S has an RO ratio in excess of expectations for star formation, but its WISE infrared colors are consistent with star-forming galaxies *without* significant AGN activity (Section 4.7). In addition, its position is nominally offset from the centroid of its (unresolved) optical counterpart at more than 3σ, but still as a probability of chance alignment of only $\sim 0.5\%$. This source is therefore promising, although we consider it more cautiously than 20181030A-S1 and 20190417A-S1 as a PRS candidate until optical spectroscopy can be obtained.

Finally, there are four radio sources with no known host optical host associations. Two have relatively high z_{max} values ($z_{max} = 0.43$ and 0.52 for 20191119A-S and 20191114A-S, respectively), and it is possible that their host galaxies are simply below the detection threshold of the optical surveys

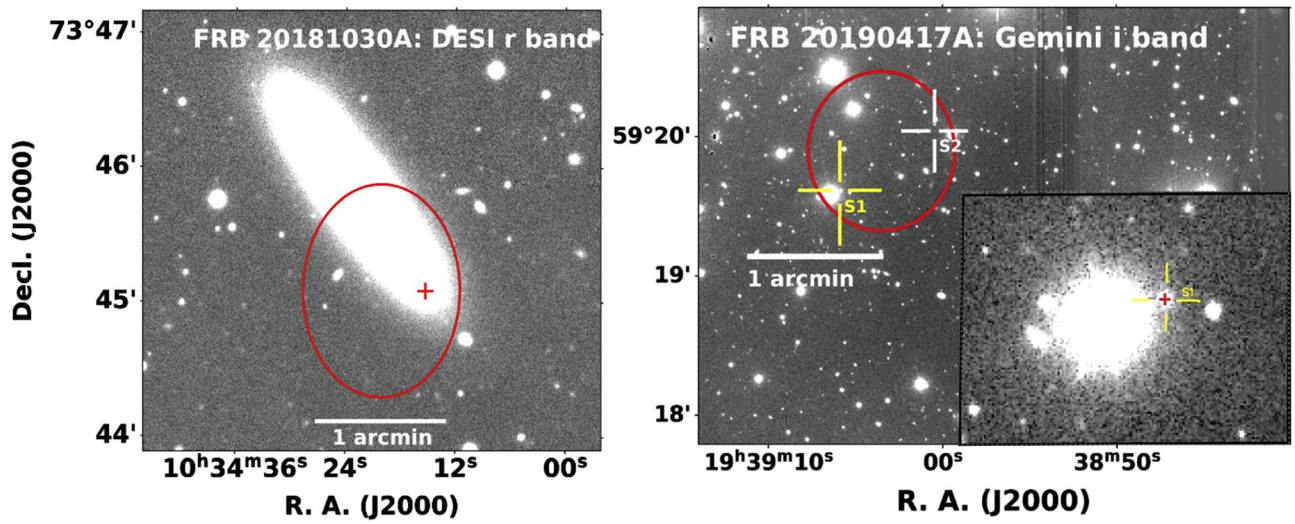

Figure 6. Optical images showing associations of the two potential radio sources from our sample. Left: DESI *r*-band field of FRB 20181030A showing the host galaxy of the FRB and the radio source—20181030A-S1. Right: Gemini North deep image of the field of FRB 20190417A. The yellow crosshair shows the location of the likely host of the radio source 20190417A-S1, which is the faint optical source near a bright star. The red "+" sign indicates the location of the radio source for both fields.

searched. At these redshifts, with a survey depth of $m \sim 24$ mag, we would only be sensitive to galaxies brighter than $M \lesssim -18$ mag. The final two sources are located in the field of FRB 20180814A. This FRB has a relatively low value of $z_{\rm max} = 0.091$ and has a most probable host-galaxy PanSTARRS-DR1 J042256.01+733940.7, as assessed by D. Michilli et al. (2023). These two radio sources are offset by 22″ and 80″ from this galaxy (which has a visible diameter in PanSTARRS of $\lesssim$10″). It is therefore probable that they are not associated with the FRB.

In conclusion, 20181030A-S1 and 20190417A-S1 are the most promising PRS candidates identified in this search to date, although we cannot fully rule out the possibility that they are (background) AGN. Additional follow-up to further explore the potential nature of these targets is ongoing. Figure 6 shows the DESI and Gemini images for 20181030A-S1 and 20190417A-S1 fields respectively with the red cross indicating the position of the radio source. In addition, while some radio sources identified (e.g., 20190110C-S, 20180814A-S2, 20180814A-S3) are unlikely to be PRSs, others (e.g., 20200619A-S) warrant further investigation to assess their viability.

5.2. Deep Limits on the Presence of PRS

While we identify a number of promising PRS candidates, future follow-up will be needed to confirm any association with the FRB. In Table 6, we therefore also quote deep limits on the flux density of any PRS, which are valid in the situation that none of the radio sources identified are linked to the FRB. We quote limits only for the fields targeted by our VLA observations described in Section 2.2.2 as these are deeper than archival surveys such as VLASS.

When computing the flux density upper limits, we take 5 times the measured rms level for the six FRBs with baseband localization regions and 3 times the measured rms level for the two FRBs with known subarcsecond localizations. Five of the eight FRBs with targeted VLA imaging also have known or most probable host galaxies presented in the literature (B. Marcote et al. 2020; M. Bhardwaj et al. 2021a, 2021b; F. Kirsten et al. 2022; D. Michilli et al. 2023). For these events, we also quote an upper limit on the spectral radio luminosity using $z_{\rm spec}$ for these galaxies. We refrain from quoting a spectral luminosity limit for the other events as they will not be significant.

Broadly, the luminosity limits presented in Table 6 are 2−4 orders of magnitude fainter than those of the two known PRSs. For the two events with subarcsecond localizations, previous limits on the presence of a PRS were available in the literature. We found the same luminosity limit for the presence of a PRS associated with FRB 20180916B as that from B. Marcote et al. (2020), but a less stringent limit for FRB 20200120E than that from F. Kirsten et al. (2022, who found $L_{\rm PRS} < 3.1 \times 10^{23}$ erg s^{-1} Hz^{-1}).

5.3. Constraints on PRS Prevalence as a Function of Luminosity and Redshift from the Global Search

In Figure 7, we summarize the key global results from our search for potential PRSs in the localization region of CHIME/FRB repeaters using both archival radio surveys (37 FRB regions searched) and targeted VLA observations (a subset of eight FRB regions searched). In particular, we plot redshift versus radio luminosity for the VLASS, VLA, and LoTSS radio detections and upper limits described above as well as the previously published PRSs (FRB 20121102A, FRB 20190520B, and FRB 20201124A). For reference, we also plot lines representing the VLASS and LoTSS sensitivity as a function of redshift.

When placing objects on this plot, we adopt a spectroscopic redshift whenever it is known and otherwise use $z_{\rm max}$ for the FRB. Points for which spectroscopic redshifts were used are outlined in red. In cases where $z_{\rm max}$ was used, these points represent upper limits on both the redshift and therefore *also* the luminosity of the radio detection/upper limit. To emphasize this, we also label these points with both horizontal and vertical arrows. (This is in contrast to points that are upper limits on the luminosity because they are derived from radio nondetections as either downward-facing triangles, diamonds, or hexagons as labeled in the legend.) The radio luminosities on this plot are calculated as $\nu L_{\nu,\alpha}$ where we have taken both the observed

Table 6
Deep Limits on PRS

FRB	Upper Limit F_ν (μJy)	σ Level[d] (σ)	Upper Lmit L_ν[a] (erg s^{-1} Hz^{-1})	z_{spec} References[e]
FRB 20180814A[c]	17.5	5	$<2.1 \times 10^{27}$	(1)
FRB 20180916B[b]	18.0	3	$<4.8 \times 10^{26}$	(2)
FRB 20181030A[c]	50.0	5	$<2.4\times10^{25}$	(3)
FRB 20190117A	80.0	5	…	…
FRB 20190208A	25.0	5	…	…
FRB 20190303A[c]	25.0	5	$<2.6 \times 10^{27}$	(1)
FRB 20190417A	42.5	5	…	…
FRB 20200120E[b]	27.0	3	$<4.2 \times 10^{23}$	(4)

Notes.
[a] The upper limit luminosities are estimated using the FRB redshifts where the FRB host is known, and its z_{spec} is available. All measurements are at 1.5 GHz.
[b] These FRBs have subarcsecond localizations, and the PRS limits here are comparable to previously published values in the literature.
[c] These FRBs have probable host galaxies identified using their CHIME/FRB baseband localizations.
[d] We measured 5σ level flux density limit for FRBs with baseband localization regions and 3σ for the ones with subarcseconds localizations.
[e] References for the z_{spec} of the published host galaxies of the FRBs. (1) D. Michilli et al. (2023), (2) B. Marcote et al. (2020), (3) M. Bhardwaj et al. (2021b), (4) M. Bhardwaj et al. (2021a), and F. Kirsten et al. (2022).

frequency and adopted redshift into account. In particular, for all observations, we calculate the spectral luminosity at a rest-frame frequency of 1.5 GHz using the equation $L_{\nu,\alpha} = \frac{4\pi D_L^2 S_\nu}{(1+z)^{1+\alpha}}\left(\frac{1.5\text{ GHz}}{\nu\text{ GHz}}\right)^\alpha$, where D_L is the luminosity distance, S_ν is the observed flux density, ν is the observed frequency, z is the source redshift, and α is the spectral index. We take $\alpha = -0.4$ (the spectral index estimated for the PRS of FRB 20121102A).

As noted above, VLASS was the deepest archival survey searched for all 37 FRB regions at GHz frequencies (where the three known PRSs were first identified). However, as can be seen in Figure 7, VLASS is only sensitive to the luminosities of previously identified PRSs at low redshift ($z \lesssim 0.11$). As only 4 of the 37 CHIME FRBs searched have z_{max} values below this, we can make only weak statements on the prevalence of PRSs with similar luminosities to that of FRB121102 based on this global search.[31] Instead, deeper targeted searches, such as those presented here for a subset of eight FRBs, will be required to make firmer statistical statements on prevalence.

However, more broadly, we can probe the possibility of more luminous FRBs than have been identified to date with all-sky surveys such as VLASS. In particular, VLASS would be sensitive to PRSs with luminosities of $\sim 10^{40}$ erg s^{-1} (a factor of $\sim$25 times more luminous than the PRS associated with FRB 20121102A) out to a redshift of $z = 0.5$. As only one of the 22 CHIME repeaters with $z_{max} < 0.5$ that were searched as part of this study even had an unresolved VLASS source in its localization region, we can conclude that such luminous PRSs must be rare (<5%). This is consistent with our finding that there is no evidence for a statistical excess of radio sources in the CHIME localization regions within these archival surveys (see Section 2.5 and Table 1).

As shown in Figure 7, the global LoTSS sensitivity in νL_ν is approximately a factor of 3.5 deeper than that of VLASS. This is due to a combination of (i) the slightly lower average survey rms (0.08 mJy beam^{-1} versus 0.12 mJy beam^{-1}, see Table 1) and (ii) the lower observing frequency coupled with the assumed negative spectral index. Given these assumptions, we would infer that LoTSS would be sensitive to PRSs with similar luminosities to FRB 20121102A out to a redshift of $z = 0.19$ (while zero of five FRB regions searched with z_{max} less than this value have an unresolved LoTSS source). In addition, based on these calculations, LoTSS would be sensitive to PRSs with radio luminosities of $\sim 10^{40}$ erg s^{-1} out to a larger redshift of $z = 0.8$. Given that only one of the 35 FRB regions searched with $z_{max} < 0.8$ had an unresolved LoTSS source, this would further decrease the estimated prevalence of such luminous PRSs to <3%.

We caution that these LoTSS constraints are dependent both on the assumed spectral index of the PRS as well as the possibility of spectral breaks at lower frequencies (which were not accounted for when placing objects on Figure 7). In particular, we note that neither of the PRSs associated with FRB 20121102A or FRB 20190520B is detected in LoTSS (while predictions based on the spectral index would place them close to the 5σ sensitivity limit of the survey). However, these results are still consistent with the conclusion that luminous PRSs are rare.

6. Comparison between Potential PRSs and FRB-PRS Models

Various models have been proposed to explain the PRS seen at the location of FRBs. Here, we examine the implication of a subset of these models in the context of the two radio sources (20181030A-S1 and 20190417A-S1) classified as potential PRSs by our analysis (Sections 6.1–6.5; see Section 5.1 for a summary of key properties of these candidates), followed by a discussion of model implications for cases where a PRS was not detected (Section 6.6). We emphasize that this analysis inherently assumes each radio source is associated with the FRB, which has yet to be confirmed. In addition, we only consider models where we have observable parameters for the radio sources that are sufficient to make an inference. Specifically, we consider four models: (i) a pulsar wind or ion–electron wind nebula, (ii) a hypernebula, (iii) an off-axis jet GRB afterglow, and (iv) SN–ejecta-CSM interaction.

For the pulsar wind or ion–electron wind nebula model (Section 6.1), both the FRB and the PRS emission are powered by the magnetar's rotational or magnetic energy. For the hypernebula model (Section 6.2), the FRB is emitted along the

[31] Since zero of these have unresolved VLASS radio sources in the field of view, we would infer that limit of <25% of repeating FRBs with $z_{max} < 0.11$ show PRSs with similar luminosity to FRB121102.

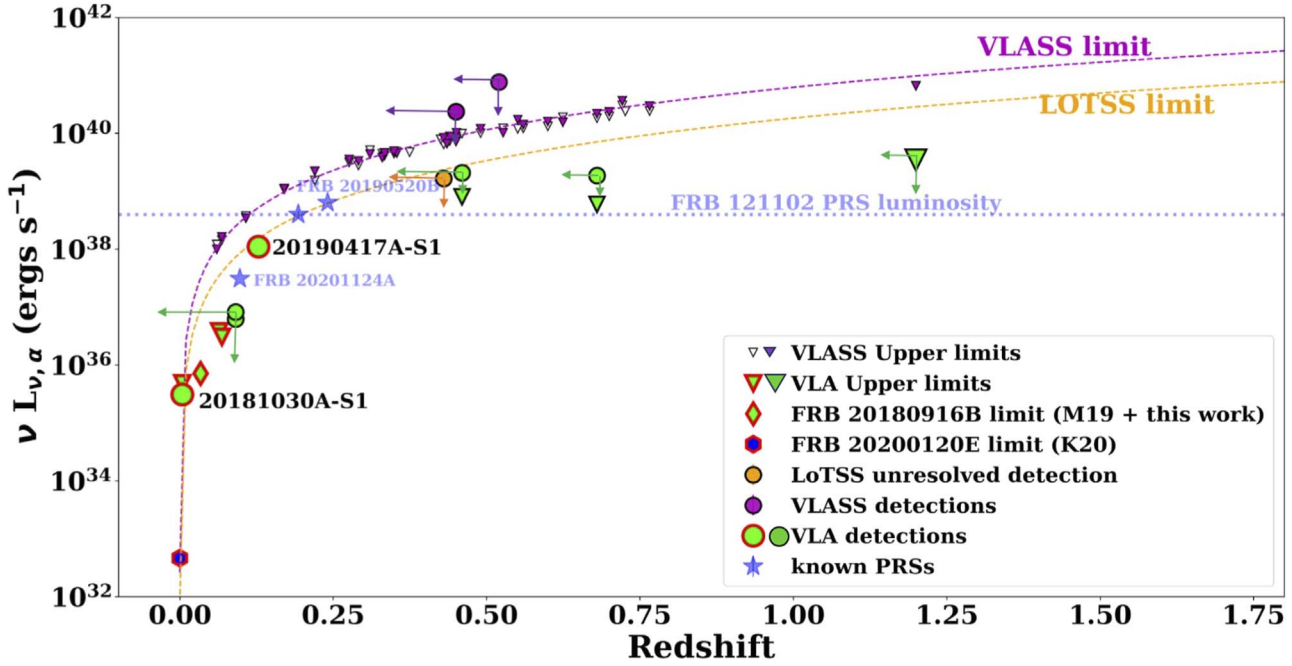

Figure 7. Luminosity vs. redshift plot showing all unresolved radio sources as circle markers from this work. The detections and deep limits obtained from VLA observations are plotted as light green inverted triangles and colored circles. The markers with red-colored marker edges are estimated with $z_{\rm spec}$ while others are estimated using $z_{\rm max}$. The luminosities shown in circles for these detections except the ones with red marker edges are considered upper limits since they were estimated using $z_{\rm max}$. In addition to the PRS of FRB 20121102A, 20190520B, and a potential PRS of FRB 20201124A (all light blue stars), we also show limits for FRB 20180916B (diamonds), and FRB 20200120E (hexagons). M19 and K20 represent B. Marcote et al. (2019) and F. Kirsten et al. (2020), respectively. The blue dotted line is the luminosity of the PRS of FRB 20121102A. Upper limits on PRSs from VLASS (small purple and white inverted triangles for first and second epochs) are also plotted, and two VLASS detections are shown as purple circles. The purple and orange dashed lines are the VLASS and LoTSS 5σ sensitivity limit as a function of redshift. The two potential PRSs from this work are shown as bigger circles with black-lettered labels: 20181030A-1 and 20190417A-1. 3σ and 5σ luminosity upper limits on the presence of a PRS are shown as inverted light green triangles for FRBs fields observed with VLA for FRBs having subarcsecond and baseband localizations respectively.

jet funnel due to magnetized shocks and reconnection events far away from the accreting engine while the PRS is powered by the interaction of the shock with the circumstellar materials released by the hyper accretion of the system. Within the off-axis jet GRB and the SN models, the FRB emission could come through the dissipation of rotational or magnetic energy from the compact object created in the explosion, while the PRS is attributed to the afterglow of a long-duration GRB (Section 6.3), or the shock interaction between the SN–ejecta and the surrounding circumstellar medium (CSM; Section 6.4).

For all models, we need the age of the radio-emitting region. Although this is unknown for the two objects considered here, we can set a lower limit based on the time of the discovery of the FRB by CHIME. For 20181030A-S1, we use the FRB discovery date (2018 October 30) to establish a lower age limit of $t_{\rm age} > 2.36$ yr (864 days) at the time of the last radio detection (2021 March 6). For 20190417A-S1, we use the FRB discovery date to estimate a lower age limit of $t_{\rm age} > 1.9$ yr (682 days) at the radio observation date (2021 February 27).

6.1. Pulsar Wind Nebula/Magnetar Ion–Electron Wind Nebula

We consider the case of a PWN or an ion–electron wind nebula as the cause of the PRS according to B. Margalit & B. D. Metzger (2018). We place constraints on the magnetic energy ($E_{\rm B}$), the age ($t_{\rm age}$), and the size (Rn) of the nebula using the luminosity and the upper limit measurement on the size of the radio source from VLA imaging at 1.5 GHz. In addition, we use the models of B. Margalit et al. (2019) to constrain the allowed ejecta properties as a function of energy injection rates, and comment on their consistency with expectations for various magnetar progenitor channels (core-collapse SNe, binary neutron star mergers, and accretion-induced collapse of WDs).

We first consider the case of 20181030A-S1. We combine the RM value of FRB 20181030A of $\sim 36.6 \pm 0.2$ rad m^{-2} (R. Mckinven et al. 2023) and the luminosity of the radio source ($L_\nu = 2.1 \times 10^{26}$ erg s^{-1} Hz^{-1}) to estimate the magnetic energy using Equation (22) of B. Margalit & B. D. Metzger (2018). We assume that the magnetization of the injected outflow, σ, is $\sim$1, and that the mean energy per particle in a proton–electron composition, χ, is 0.2 GeV. This yields estimates for the magnetic energy of $E_{\rm B} \sim 2.9 \times 10^{46}$ erg s^{-1} Hz^{-1} and magnetic field strength of $B \sim 2.26 \times 10^{14}$ G. We then calculate an upper limit on the age of the nebulae of $t_{\rm age} < 3011$ yr using $t_{\rm age} \sim E_{\rm B}/\nu L_\nu$ (ν is the 1.5 GHz frequency of the radio observations).

To estimate the upper limit on the true size of the nebula, we use the beam size of the combined VLA image of the radio source, which is 1.″1 for the semimajor axis. At the angular diameter distance of the galaxy ($D_{\rm A} \sim 17$ Mpc), we obtained an upper limit on the size of the nebula to be <92 pc. R. Mckinven et al. (2023) reported a high linear polarization fraction and varying polarization angle from the RM analysis for this FRB. This means that the FRB is likely coming from the neighborhood of its central engine if powered by a magnetar (R. Mckinven et al. 2023), similar to the "nearby" or magnetospheric models of FRB (K. Murase et al. 2016; P. Kumar et al. 2017; P. Kumar & Ž. Bošnjak 2020; P. Kumar et al. 2024).

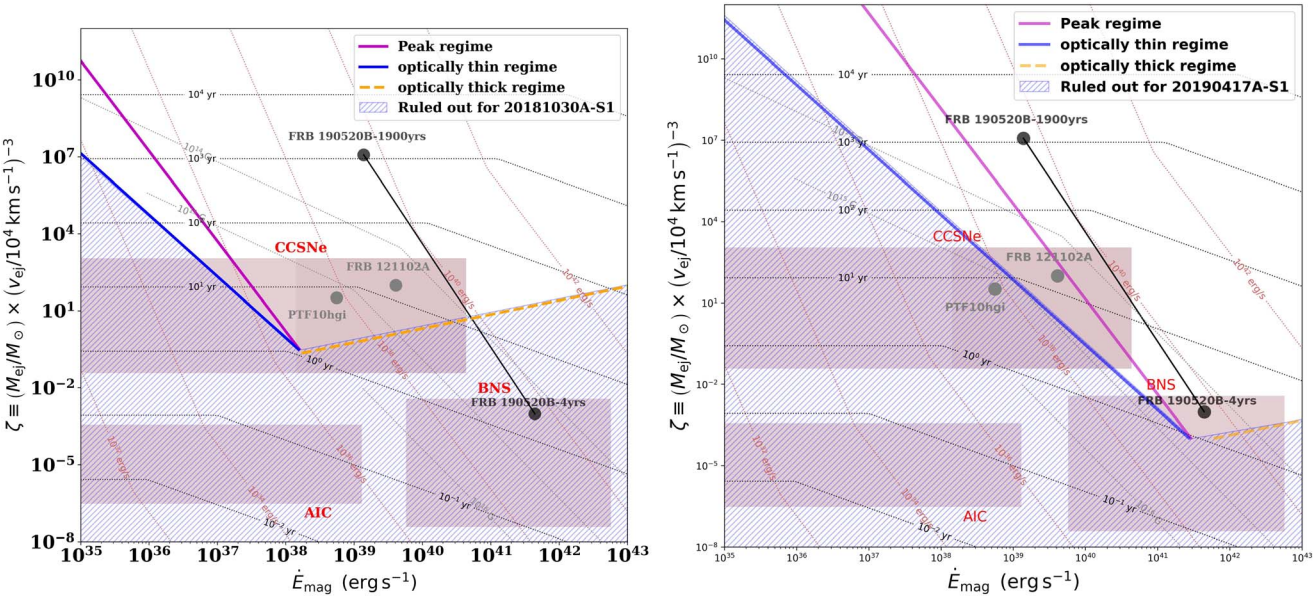

Figure 8. Characteristics of the nebular radio emission emitted by magnetars originating from diverse progenitor pathways such as a superluminous supernovae (SLSNe), a long gamma-ray bursts (LGRB), a binary neutron star (BNS) merger, or accretion-induced collapse (AIC) of a white dwarf for 20181030A-S1 (left) and 20190417A-S1 (right). For the different regimes predicted by our model, the blue-shaded regions correspond to the parameter spaces ruled out for 20181030A-S1 and 20190417A-S1 respectively. The allowed ejecta density parameter space for 20181030A-S1 is consistent with magnetars born through core collapse, i.e., SLSNe and LGRB while that of 20190417A-S1 is consistent with core-collapse SN and binary neutron star mergers. The properties of the PRS of FRB 20121102A (B. Margalit et al. 2019) and FRB 20190520B (S. Bhandari et al. 2023b) are also overplotted and consistent with the unshaded regions of the parameter space of 20181030A-S1 and 20190417A-S1.

Next, we can estimate the allowed parameter space for the ejecta density parameterized by $\zeta = (M_{ej}/M_\odot) \times (v_{ej}/10^4\,km\,s^{-1})^{-3}$ assuming a range of energy injection rates, $\dot{E}_{mag}$, where M_{ej} is the ejecta mass, and v_{ej} is the ejecta velocity of the event. To do this, we solved the analytic equations for synchrotron radiation assuming the detected 1.5 GHz radio emission was in one of three regimes: (i) in the optically thick regime, (ii) at peak frequency, and (ii) in the optically thin regime. These are represented in Equations (19), (23), and (21) of B. Margalit et al. (2019) respectively. The left panel of Figure 8 shows the result of this analysis using the spectral luminosity of 20181030A-S1. When we consider the lower age limit constraint of >3 yr (based on the time between the FRB discovery the the radio observations), the remaining allowed parameter space is shown as an unshaded region. We also note that the lower peak regime and the optically thick regime are ruled out by the measured in-band spectral index of ~ -0.7 (Section 4.3).

According to the allowable parameter range, the binary neutron star and accretion-induced collapse models are ruled out as a potential source of the magnetar if 20181030A-S1 is associated with the FRB. For comparison, the parameter estimation for the PRS of FRB 20190520B from S. Bhandari et al. (2023b) is also displayed, where the two ends of the line correspond to its lower and upper age limits (with constraints from the lower limit aligning with the parameter space estimated for magnetar formed by a binary neutron star merger). Alongside FRB 20121102A, the PRS candidate identified here for FRB 20181030A suggests consistency with magnetars formed in SLSNe/LGRB—ruling out binary neutron star mergers and accretion-induced collapse of a white dwarf.

We next follow the same procedure for the radio source 20190417A-S1. We note that the high and varying RM of this FRB (4681–4429 rad m^{-2}; Y. Feng et al. 2022; R. Mckinven et al. 2023) includes other repeaters (including FRB 20121102A, S. Chatterjee et al. 2017; and FRB 20190520B, C. H. Niu et al. 2022) that are probably residing in dynamic magnetoionic environments, and makes this radio source an object of particular interest. We obtain estimates of $E_B \sim 2.11 \times 10^{50}$ erg s^{-1} Hz^{-1}, $B \sim 1.9 \times 10^{16}$ G, and an upper limit on $t_{age} < 56{,}186$ yr. We then use the beam size of the combined VLA image of the radio source, which is 1.″3 for the semimajor axis at an angular diameter distance of $D_A \sim 475.5$ Mpc, to obtain an upper limit on the size of the nebula to be <3.2 kpc ($<9.75 \times 10^{21}$ cm). When considering the allowed ejecta parameters as a function of energy injection (see the right panel of Figure 8), our analysis yields a range of parameter spaces consistent with core-collapse SN and binary neutron star mergers. In the future, accurate measurements of the sizes of the radio sources via the VLBI method and a well-defined spectral energy distribution (SED) could yield tighter constraints for both 20181030A-S1 and 20190417A-S1.

6.2. Hypernebula Model

Another paradigm proposed to self-consistently explain the observed properties of FRBs and their associated PRS is a hypernebula that is inflated by the baryon-rich outflows ejected by hyperaccreting compact objects (N. Sridhar & B. D. Metzger 2022; N. Sridhar et al. 2024). Recently, this model was employed to explain the observed properties of FRBs 20210117A (S. Bhandari et al. 2023a), 20201124A (Y. Dong et al. 2024a), and 20190520B (S. Bhandari et al. 2023b). In this picture, the FRB is emitted along the jet funnel due to magnetized shocks and reconnection events far away from the accreting engine (N. Sridhar et al. 2021). We investigate the possibility of this model here in light of our observations.

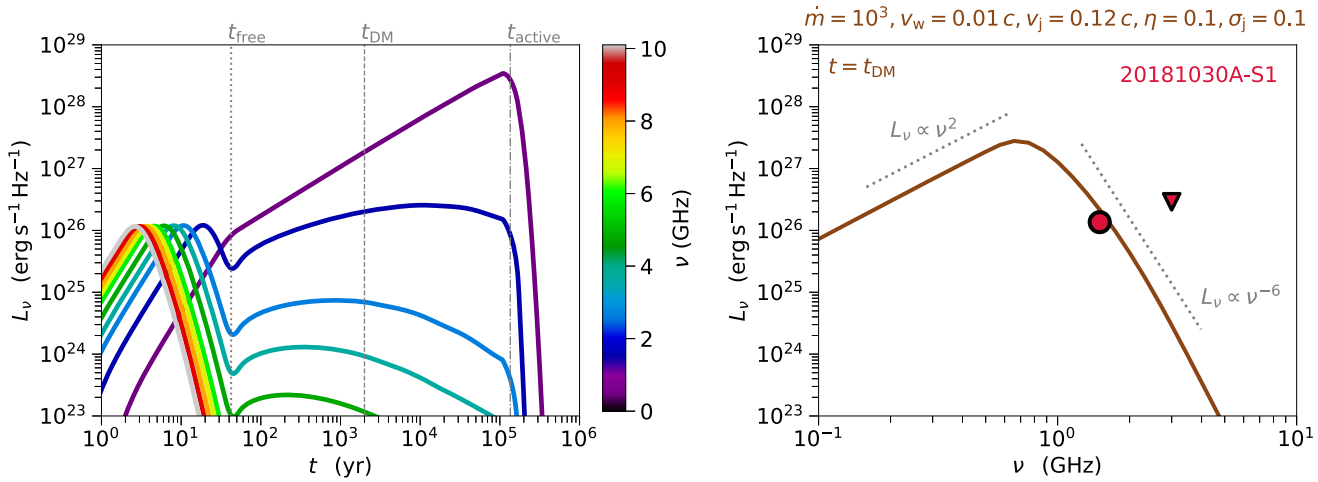

Figure 9. Radio synchrotron emission from an accretion-powered hypernebula surrounding the FRB 20181030A. Left panel: Light curves of the expanding hypernebula in different bands (color-coded). Vertical gray dotted, dashed, and dashed–dotted lines denote the free-expansion timescale of the hypernebula (Equation (1)), the moment during the evolution when the contribution of the hypernebula material to the DM matches the observed $DM_{\rm host}$, and the active duration of the central accreting engine $t_{\rm active}$, respectively (see Section 6.2 for more details on the system's parameters). Right panel: Spectral energy distribution at $t = t_{\rm DM} \sim 2000$ yr. The red markers are the observed spectrum (downward-facing triangle is an upper limit) of the proposed PRS associated with FRB 20181030 A.

We first consider 20181030A-S1. We take the maximum isotropic-equivalent luminosity of FRB 20181030A to be $10^{40}\,{\rm erg\,s^{-1}}$ (CHIME/FRB Collaboration et al. 2019); this requires an accretion rate of $\dot{M}_\bullet \gtrsim 10^3 \dot{M}_{\rm Edd}$ for the FRB to be accretion-jet powered (N. Sridhar et al. 2021), where $\dot{M}_{\rm Edd} \sim 1.3 \times 10^{39}\,{\rm erg\,s^{-1}}$ is the Eddington mass transfer rate for an accreting $10\,M_\odot$ black hole (or a requirement of $\dot{M}_\bullet \gtrsim 10^4 \dot{M}_{\rm Edd}$ for the FRB to be powered by a neutron star). The large-angled, slower disk winds (with speeds $v_{\rm w} \sim 0.01c$, and mass-loss rate $\dot{M}_{\rm w} \sim \dot{M}_\bullet$) powered by the hyperaccreting disk will drive a forward shock into the CSM (with an assumed density $n \approx 10\,{\rm cm^{-3}}$). The compact object also powers a faster wind/jet along the spin axis (with speeds $v_{\rm j} \sim 0.12c$) that drives the termination shock upon interaction with the slower disk winds.

Following N. Sridhar & B. D. Metzger (2022), we calculate the observable properties of the hypernebula due to these interactions for the following assumed physical parameters: the jet magnetization parameter (ratio of the magnetic enthalpy density to the plasma enthalpy density) $\sigma_{\rm j} = 0.1$, the ratio of the wind luminosity to the jet luminosity $\eta = 0.1$, the fraction of the shock power that goes into heating the electrons $\varepsilon_{\rm e} = 0.5$, the mass of the accreting compact object $M_\bullet = 10\,M_\odot$ (assuming a black hole), and the mass of the companion accretor star $M_\star = 30\,M_\odot$: this sets the active lifetime of the system to be $t_{\rm active} \sim M_\star/\dot{M}_\bullet$. The radio synchrotron light curves from the hypernebula at different bands are provided in the left panel of Figure 9.

The free-expansion timescale of the outflowing winds (before they start to decelerate) is

$$t_{\rm free} \approx 42\ {\rm yr} \left(\frac{L_{\rm w,39}}{n_1}\right)^{1/2} \left(\frac{v_{\rm w}}{0.01\ c}\right)^{-2.5}. \quad (1)$$

Here, we adopt the shorthand notation, $Y_x \equiv Y/10^x$ for quantities in cgs units. The contribution of the expanding shell to the DM (assuming the shell remains ionized) bridging the free-expansion and deceleration phases is

$$\begin{aligned} {\rm DM_{sh}} &\simeq \frac{M_{\rm sh}}{4\pi R^2 m_{\rm p}} \\ &\approx \begin{cases} 1\ {\rm pc\ cm^{-3}} \left(\dfrac{\dot{M}_{\rm w}}{10^3 \dot{M}_{\rm Edd}}\right) v_{\rm w,9}^{-2} \left(\dfrac{t}{42\ {\rm yr}}\right)^{-1} & (t < t_{\rm free}) \\ 1\ {\rm pc\ cm^{-3}} \left(\dfrac{L_{\rm w,39}}{n_1}\right)^{1/5} \left(\dfrac{t}{42\ {\rm yr}}\right)^{3/5} & (t > t_{\rm free}), \end{cases} \end{aligned} \quad (2)$$

where we take the mass in the expanding shell to be $M_{\rm sh} \sim \dot{M}_{\rm w} t$, and $m_{\rm p} = 1.67 \times 10^{-24}\,g$ is the proton's mass.

The host contribution to the DM for FRB 20181030A is estimated to be ${\rm DM_{host}} \sim 10\,{\rm pc\,cm^{-3}}$ (M. Bhardwaj et al. 2021b). The hypernebula shell will contribute this value of DM when the hypernebula's age is $t_{\rm DM} \sim 2000$ yr. The aforementioned three timescales are indicated by gray dotted ($t_{\rm free}$), dashed ($t_{\rm DM}$), and dashed–dotted ($t_{\rm active}$) vertical lines in the left panel of Figure 9. We compute the radio synchrotron spectrum at time $t_{\rm DM}$, which is shown as a brown curve in the right panel of Figure 9. We note that the hypernebula model spectrum is consistent with the observations (red markers). Furthermore, in this model, the expected X-ray flux from the accretion disk—during the active period of FRB emissions when the accreting cone is aligned with the observer—is expected to be $<2 \times 10^{-11}\,{\rm erg\,s^{-1}\,cm^{-2}}$ (taking a distance of 20 Mpc and X-ray luminosity of $\lesssim 10^{42}\,{\rm erg\,s^{-2}}$). This is also consistent with the X-ray flare upper limits of $\lesssim 10^{46}\,{\rm erg\,s^{-1}}$ (M. Bhardwaj et al. 2021a).

We next consider 20190417A-S1. A peak radio burst luminosity of $10^{41-42}\,{\rm erg\,s^{-1}}$ from FRB 20190417A (adopting FRB fluxes from E. Fonseca et al. 2020 and a redshift of $z = 0.12817$ corresponding to the PRS candidate 20190417A-S1 presented here) would require an accreting engine transferring matter at $\dot{M}_\bullet \gtrsim 10^{4-5}\,\dot{M}_{\rm Edd}$. A hypernebula powered by such an engine could contribute to a large ${\rm DM_{host}} \lesssim 1250\,{\rm pc\,cm^{-3}}$ at the age of $t \sim 7$ yr (Equation (2)). This is consistent with the observed upper limit on $\rm DM_{host}$ of

FRB 20190417A that one can obtain by roughly subtracting the Milky Way and host-galaxy contributions (E. Fonseca et al. 2020). At this age, the hypernebula shell would still be in the free-expansion phase (Equation (1)), and the nebula could contribute to a large maximum RM ($\mathrm{RM} \lesssim 10^7\,\mathrm{rad\,m^{-2}}$; see Equation (50) of N. Sridhar & B. D. Metzger 2022), which may be consistent with the current measurements of $\mathrm{RM} \sim 4681\,\mathrm{rad\,m^{-2}}$ (R. Mckinven et al. 2023). These properties resemble that of FRBs 20121102A and 20190520B, which were also explained using the hypernebula model (N. Sridhar & B. D. Metzger 2022; S. Bhandari et al. 2023b). However, due to the uncertain value of the $\mathrm{DM_{host}}$ associated with FRB 20190417A (E. Fonseca et al. 2020), and a lack of a robust distance/host-galaxy association between FRB 20190417A and PRS 20190417A-S1, we defer from performing a detailed spectral analysis for PRS 20190417A-S1 (in a way that is self-consistent with the properties of the FRB).

6.3. Off-axis Jet Afterglow Model from LGRB/SLSN

Next, we explore the off-axis jet afterglow model as a possible alternative source of PRS emission. Specifically, we examine whether it is possible to explain the radio sources 20181030A-S1 and 20190417A-S1 with parameters broadly consistent with those observed for other GRBs. We used the open-source Python package `afterglowpy` (G. Ryan et al. 2020)—software that uses numerical models to calculate structured jet afterglows, synthetic light curves, and spectra from any viewing angle. We run a dense grid of isotropic-equivalent jet energies, $E_{\rm iso}$, and interstellar material (ISM) densities, n, through and calculate radio light curves for each pair at three viewing angles, $\theta_{\rm obs} = 30°$, 60°, 90°.

Following previous GRB studies (e.g., K. D. Alexander et al. 2017; T. Laskar et al. 2019; T. Eftekhari et al. 2021), we assume a Gaussian jet type, a 10° half-opening angle, a truncation angle that is 5 times the opening angle, an electron energy distribution index of 2.6, and fractional values for postshock energy contained in the relativistic electrons (ϵ_e) and amplified magnetic fields (ϵ_b) set at 0.005 and 0.01, respectively. Additionally, we fix the fraction of accelerated electrons (X_n) at 0.8.

For each model in our grid, we generate light curves at 1.5 GHz and compare them with our radio detections. We consider a given model to be "allowed" if it passes through the observed radio flux within its 1σ uncertainty and ruled out if it does not. We adopt ages of 864 and 682 days for 20181030A-S1 and 20190417A-S1, respectively. These correspond to lower limits on their true age, as described above. In Figure 10, we plot the allowed values of $E_{\rm iso}$ and n at each viewing angle considered for both events.

For 20181030A-S1, we find that the radio constraints mostly allow the possibility of jets with energies $7 \times 10^{52}\,\mathrm{erg} \leqslant E_{\rm iso} \leqslant 2 \times 10^{53}\,\mathrm{erg}$ at $n \sim 10^{-2}$–$10^{2}\,\mathrm{cm^{-3}}$ for viewing angles, $\theta_{\rm obs} = 30°$ and 60°. However, for the same ISM densities, we are unable to rule out the jet energies $E_{\rm iso} \geqslant 4 \times 10^{52}\,\mathrm{erg}$ for $\theta_{\rm obs} = 90°$. For 20190417A-S1, we have a tight range of allowable energies from $(1.39\ \mathrm{to}\ 1.84) \times 10^{54}\,\mathrm{erg}$ for $\theta_{\rm obs} = 30°$. However, we are unable to rule out jet energies $\geqslant 9 \times 10^{53}\,\mathrm{erg}$ and $\geqslant 5 \times 10^{53}\,\mathrm{erg}$ for $\theta_{\rm obs} = 60°$ and $\theta_{\rm obs} = 90°$ respectively.

Our results for 20181030A-S1 are consistent with previously reported GRB afterglows at a similar frequency (e.g., E. Berger et al. 2003; D. A. Frail et al. 2005; L. Resmi et al. 2005; S. B. Cenko et al. 2010). However, the resultant jet energies for 20190417A-S1 are higher than previously reported radio afterglow limits except for the ultralong GRB 111209A (G. Stratta et al. 2013). However, we emphasize that these constraints can be more robust with a well-defined light curve or SED and are highly sensitive to the adopted $t_{\rm age}$.

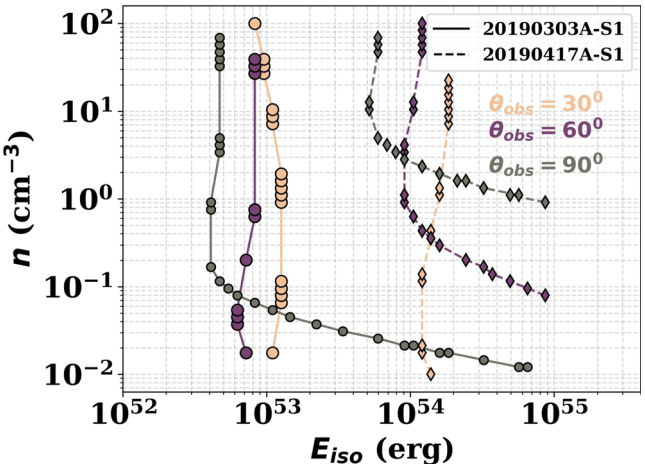

Figure 10. Some allowable parameter space for the properties of 20181030A-S1 (circles) and 20190417A-S1 (diamonds) if they are each a radio afterglow from an off-axis jet of a long gamma-ray burst or a superluminous supernova associated with their FRBs. The allowed range of energies for 20190417A-S1 is consistent with higher values when compared to that of 20181030A-S1 for the same range of ISM densities.

6.4. Supernova Ejecta Model

Finally, we consider a radio SN or a young SN remnant as the cause of the radio emission. Radio emission originating from interacting SNe predominantly arises from synchrotron radiation at the forward shock, formed by the fastest-moving ejecta, as the SN shockwave collides with the CSM (e.g., PTF10hgi; T. Eftekhari et al. 2019).

We employ a modified version of the framework outlined by R. A. Chevalier (1998) and R. A. Chevalier & C. Fransson (2006) to model the radio SED of the radio source, focusing on SE from interacting SNe. Specifically, our model accounts for the influence of both synchrotron self-absorption (SSA) and free–free absorption (FFA), as described in Ibik et al. (2024). Throughout our modeling, we assume baseline values for constants and free parameters. In particular, we assume the equipartition of energy ($\alpha = 1$), the radio filling factor $f = 0.5$, and the fraction of postshock energy contained in amplified magnetic fields of $\epsilon_b = 0.1$.

To investigate the implications of the VLA radio detection and VLASS upper limit[32] for the 20181030A-S1 and 20190417A-S1, we generate a dense grid of SSA+FFA SEDs for a wide range of peak fluxes (0.001−10 mJy) and frequencies (0.05−50 GHz). When constructing the SED grid, we apply values for the free–free optical depth that assume a wind-like medium for the external CSM (see Ibik et al. 2024). For each SED, we then determine whether it is consistent with,

[32] We note to use the flux density limit from the VLASS second epoch of observation. While these are not contemporaneous with the VLA observations, they were observed within 5–6 months, and old radio SN are expected to be relatively slowly evolving.

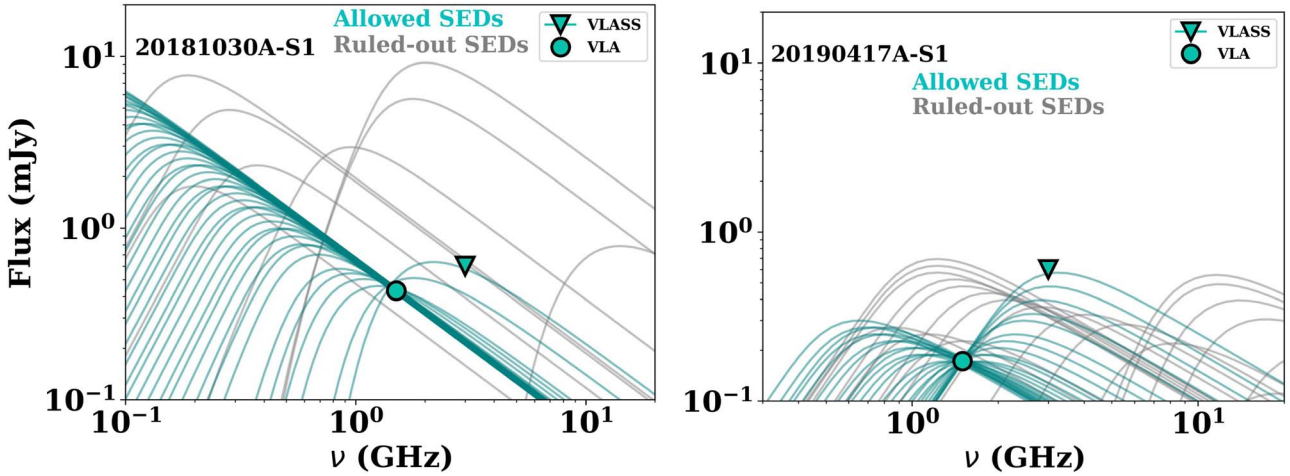

Figure 11. Model SEDs of the radio source, 20181030A-S1 (left panel) and 20190417A-S1 (right panel), assuming an expanding SN ejecta colliding into external CSM. The cyan-colored lines are the allowed SEDs given the model. We report the corresponding allowed parameter space for the properties of the explosion in Section 6.4, which are consistent with a moderately luminous supernova.

or ruled out by VLA radio detection. The left panel of Figure 11 shows examples of allowed (cyan) and ruled-out (gray) SEDs for 20181030A-S1.

For each allowed SED, we can then take the peak frequency, and peak flux and infer a radius for the radio-emitting region. When further coupled with an assumption for the age of the transient, we can also constrain the SN shock velocity and the density of the circumstellar material. Given that we have only a single detection, the peak of the SED could be at arbitrarily low frequencies (see Figure 11)—as a result, our models are unconstrained at the high radius/velocity side. However, if we adopt an age of 864 days (which is formally a lower limit; see above) and restrict ourselves to solutions with velocities < 0.3 c (as is typical for SN), then we would infer a radius for the radio-emitting region of $\sim(2-70) \times 10^{16}$ cm and CSM density of $\sim 3 \times 10^{-25}$ -9×10^{-20} g cm^{-3}. In this scenario, allowed shock velocities range from $\sim$3500 km s^{-1} to our imposed upper limit. Broadly, these parameters are consistent with those observed for all types of core-collapse SN.

We apply a similar approach to the VLA detection and VLASS upper limit for 20190417A-S1 and show a set of example allowed and ruled-out SED in the right panel of Figure 11. As above, the radii and velocities are unconstrained on the high end. However, adopting an age of 682 days (a lower limit) and restricting ourselves to solutions with shock velocities $< 0.3c$, we would infer a radius of the radio-emitting region of $\sim(1-5) \times 10^{17}$ cm and CSM density of $\sim 10 \times 10^{-24}$ -6×10^{-21} cm^{-3}. In this scenario, the allowed shock velocities range from $\sim 2 \times 10^4$ km s^{-1} up to our imposed upper limit. Such high shock velocities are not expected for normal core-collapse SN, but are instead closer to those found for some Type Ibc SN (e.g., SN2008D, D. Malesani et al. 2009) including the "broad-lined" subgroup. However, given that the explosion epoch used here is a lower limit on the age of the radio source, the inferred shock velocities could be lower (if the transient were older). Thus, overall, we find that, given the uncertainty in both the age and spectral shape of 20181030A-S1 and 20190417A-S1, either could be consistent with emission from an SN.

6.5. Summary of Models for 20181030A-S1 and 20190417A-S1

In the sections above, we considered four theoretical models for PRS emission: (i) a pulsar wind or ion–electron wind nebula, (ii) a hypernebula, (iii) an off-axis jet GRB afterglow, and (iv) SN–ejecta–CSM interaction. Broadly, we find that—within current constraints—any of these models could explain the luminosity of the radio sources 20181030A-S1 and 20190417A-S1. However, we note that some of these results are highly model dependent. For example, in the magnetar model, the size of the nebula would be strongly dependent on the source age ($t_{\rm age}$), for which we only have lower limits. In addition, for both the GRB and SN models, the observed radio emission can be explained using parameters similar to those seen in some SNe and GRBs. However, this explanation is highly contingent on several uncertain factors, particularly the true age ($t_{\rm age}$) of the event and the spectral shape. Depending on these variables, the models may become incompatible, but we cannot dismiss them as a potential source for the emission at this stage.

However, it is notable that several properties of both the FRBs and the candidates PRSs presented in this work are consistent with expectations for a nebular origin for PRSs. In particular, in Figure 12, we plot the spectral luminosities and RMs of the two potential PRSs from this work alongside other previously published PRSs and upper limits. We see that both 20181030A-S1 and 20190417A-S1 align well with the nebula model framework as predicted and shown by Y.-P. Yang et al. (2020) and G. Bruni et al. (2024). If 20181030A-S1 and 20190417A-S1 are confirmed to be associated with the FRBs, future work examining both FRB properties (e.g., activity[33]) and PRS properties (e.g., size) can further assess their consistency with this picture.

[33] We note that, despite the relatively young predicted ages for these sources within the magnetar and hypernebulae models, FRBs 20181030A and 20190417A are not among the most active FRB repeaters discovered by CHIME (with 9 and 19 bursts detected, respectively). However, this does not preclude them from being young and active FRBs. For instance, we highlight that only one burst from FRB 20121102A has been detected by CHIME to date.

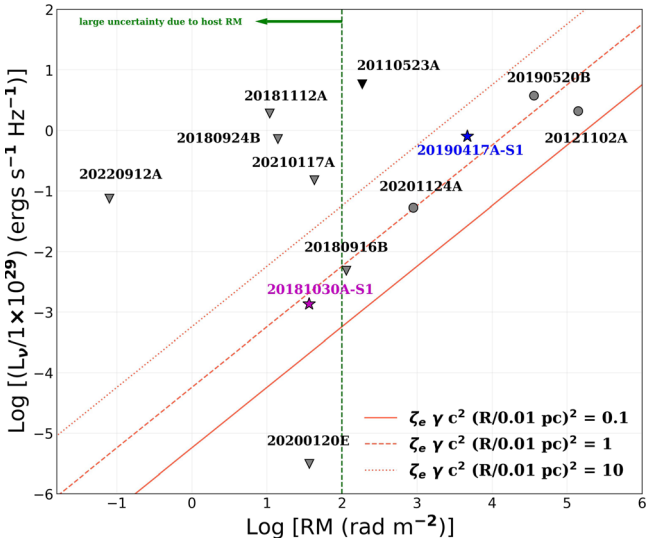

Figure 12. The proposed relation between specific radio luminosity of PRS and the FRB rotation measure adapted from G. Bruni et al. (2024). The colored stars and inverted triangles are potential PRSs (20181030A-S1 and 20190417A-S1) and upper limits from our sample (20190117A-S and 20190208A-S). The pink dotted, dashed, and solid lines are predicted relations of values 0.1, 1, and 10 from the nebula model framework. Gray circles are values for the three known PRSs while the inverted gray triangles are PRS upper limits for those FRBs.

6.6. Physical Implications for Nondetections of PRSs

In Figure 7, we presented the upper limits for VLASS nondetections in the majority of the searched FRB repeater fields. In Section 5.3, we used these limits to conclude that PRSs with high luminosities ($\sim 10^{40}$ erg s^{-1}, which is $\sim$25 times brighter than the PRS associated with FRB 20121102) must be rare. This high radio luminosity exceeds what has been observed from SLSNe and LGRBs (at times >100 days) to date (T. Eftekhari et al. 2021; Ibik et al. 2024). We would therefore not expect to see such bright radio emission, except in very extreme cases, if these sources are the origin of the PRS emission. However, in the context of nebular models, it is theoretically possible to achieve these high luminosities in environments with extremely strong magnetic fields and super-Eddington accretion rates (B. Margalit & B. D. Metzger 2018; N. Sridhar et al. 2021, 2024), although no such environments have been observed.

We also established deep PRS flux limits for a subset of these FRBs. Notably, for five FRBs with known redshifts (all below $z < 0.1$), these limits are 2−6 orders of magnitude fainter than the PRS of FRB 20121102A. This suggests that these FRBs either lack associated PRSs or have PRSs that are significantly less luminous than that of FRB 20121102A. This has important implications for the nature of FRBs that should have PRSs. Although the small sample size of known PRSs limits our understanding, we discuss the following factors that may influence whether we can detect a PRS if associated with a repeating FRB (see also discussions offered by B. Marcote et al. 2020; F. Kirsten et al. 2022; J. O. Chibueze et al. 2022):

1. *Age*. Aging PRS sources may enter a quiescent phase, causing their emission to weaken and become undetectable. This is due to the shutdown of energy injection from a central engine (e.g., B. Margalit & B. D. Metzger 2018).
2. *Timing of observation.* For periodic and randomly variable sources, observing a PRS during a quiescent period may result in nondetection (for example, this has been seen in pulsars; D. R. Lorimer & M. Kramer 2004).
3. *Beaming*. Another possibility is that the PRS emission is beamed, and if we are not observing from the optimal angle, the PRS may remain undetected (G. B. Rybicki & A. P. Lightman 1986).
4. *Burst rate*. Certain FRB-PRS models, including the synchrotron maser and hypernebula models, suggest a positive correlation between burst rate and PRS luminosity. This correlation is thought to arise from an increased electron–ion injection rate, fueling maser emission (B. D. Metzger et al. 2019), or an increased accretion rate fueling SE (N. Sridhar et al. 2021). According to these models, FRBs with low burst rates would be expected to have faint PRSs, potentially evading detection due to instrumental sensitivity limitations. The possibility of such a correlation will be explored in an upcoming work (M. Bhardwaj et al. 2024, in preparation).
5. *Environment*. Local environmental conditions, such as magnetic field strength, relativistic electron density, electron–ion injection rate, and accretion rate are crucial for SE. Generally, even with a strong magnetic field, insufficient relativistic electrons can prevent radio emission. In the nebular scenario, the energy density in the surrounding environment is key, as it influences the correlation between FRB RM and PRS luminosity, as predicted by Y.-P. Yang et al. (2020) and observed in some FRBs by G. Bruni et al. (2024; see Section 6.5 and Figure 12). This suggests that FRBs with low RM may not exhibit a PRS due to a weaker magnetoionic medium, hindering emission (G. Bruni et al. 2024).

Some of these factors described above, specifically the burst/repetition rate and RM of FRBs, could inform future follow-up observations of FRB repeater fields and searches for their PRSs.

7. Summary and Conclusions

We have conducted a comprehensive search for and characterization of radio sources within the $\sim 1'$ baseband localization regions of 37 repeating FRBs discovered by CHIME/FRB. This is part of an ongoing effort to identify additional PRSs similar to those that have been found at the location of two confirmed repeating FRBs to date. We search archival radios' surveys for all 37 FRBs and supplement this with deeper, targeted VLA observations of the localization region for a subset of eight events. In total, we identify 25 radio sources (13 in archival surveys and 12 from deep VLA observations) within the fields of 14 of the FRBs. Of these, 10 radio sources were unresolved (as would be expected for true PRSs) while the rest were extended/resolved. We summarize the rest of our findings as follows:

Multiwavelength characterization. We perform multiwavelength characterization of the 10 unresolved radio sources identified in our search—with an emphasis on six sources with detected optical counterparts/host associations. We examine properties such as host redshift, radio variability, and spectral shape, host-galaxy offset, probability of chance alignment, optical-to-radio ratio, infrared colors, and host SFRs. Our goal

was to identify any radio sources that (i) appear to be inconsistent with expectations for either star formation or an AGN in the host galaxies, and (ii) have properties broadly comparable to the previously identified PRSs.

Candidate PRSs. After conducting our multiwavelength analysis, we identify two radio sources of particular interest for which we disfavor either a star formation or host AGN origin. 20181030A-S1 overlaps with the spiral arm of NGC 3252, which was previously identified as the most likely host of FRB 20181030A (M. Bhardwaj et al. 2021b). If located in the galaxy, it has a radio luminosity of approximately 3 orders of magnitude fainter than the PRS of FRB 20121102A. In contrast, 20190417A-S1 is associated with a star-forming galaxy at a redshift of $z = 0.128$ and has a luminosity broadly similar to that of the FRB 20121102A PRS. Both sources have nonthermal spectral indices.

Deep limits. We present deep radio limits on the presence of a PRS for the eight FRBs with targeted VLA imaging. We include the fields of the PRS candidates in the case that these radio sources are not truly associated with the FRBs. These limits are generally 2–4 orders of magnitude fainter than the PRS associated with FRB 20121102.

Implication of global search. We also consider the global implications of our search of 37 CHIME/FRB localization regions on the prevalence of PRSs. VLASS was the deepest radio survey at GHz frequencies but is only sensitive to PRSs with similar luminosities to FRB 20121102A out to a redshift of $z \sim 0.1$. Hence, deeper targeted observations are necessary to probe such objects. However, VLASS would be sensitive to PRSs with radio luminosities of $\sim 10^{40}$ erg s^{-1} out to a redshift of $z \sim 0.5$. Based on the lack of detected VLASS sources in fields with $z_{\rm max}$ less than this, we conclude such luminous PRSs must be rare (<5% of repeaters).

Comparison to FRB-PRS models. Finally, we explored the implications for the two candidate PRSs identified here within the framework for four FRB-PRS models. Broadly, we found that it was possible to explain the radio detections with reasonable parameters in any of the (i) PWN/magnetar ion–electron wind nebulae, (ii) hypernebulae, (iii) GRB afterglow, or (iv) SN–ejecta-CSM interaction models. However, we note that both objects are consistent with the expected PRS luminosity versus RM relationship expected with the model nebulae framework (Y.-P. Yang et al. 2020; G. Bruni et al. 2024), and the hypernebulae model can also broadly explain the amount of excess DM inferred for both events if they are associated with the FRB. Future observations with more constraining size estimates and SEDs for both sources would be able to further refine and potentially exclude a subset of models.

Overall, the analyses in this manuscript are clues to finding PRSs in the coming era of CHIME/Outriggers (C. Leung et al. 2021; T. Cassanelli et al. 2022; J. Mena-Parra et al. 2022; A. E. Lanman et al. 2024), DSA-110 (V. Ravi et al. 2023), and MeerTrap (K. M. Rajwade et al. 2022). We emphasize that we do not claim any associations between the potential PRSs with their FRBs. We recommend following up on these FRBs to confirm or rule out any of these potential PRSs, particularly by localizing subsequent bursts to ∼arcsecond precision.

Acknowledgments

We acknowledge Gabriele Bruni and Yuan-Pei Yang for their useful conversations.

We acknowledge that CHIME is located in the traditional, ancestral, and unceded territory of the Syilx/Okanagan people. We are grateful to the staff of the Dominion Radio Astrophysical Observatory, which is operated by the National Research Council of Canada. CHIME is funded by a grant from the Canada Foundation for Innovation (CFI) 2012 Leading Edge Fund (project 31170) and by contributions from the provinces of British Columbia, Quebec, and Ontario. The CHIME/FRB Project is funded by a grant from the CFI 2015 Innovation Fund (project 33213) and by contributions from the provinces of British Columbia and Quebec, and by the Dunlap Institute for Astronomy and Astrophysics at the University of Toronto. Additional support was provided by the Canadian Institute for Advanced Research (CIFAR), McGill University, and the McGill Space Institute thanks to the Trottier Family Foundation and the University of British Columbia. The CHIME/FRB baseband system is funded in part by a Canada Foundation for Innovation John R. Evans Leaders Fund award to IHS.

The National Radio Astronomy Observatory (NRAO) is a facility of the National Science Foundation operated under a cooperative agreement by Associated Universities, Inc. We would like to acknowledge NRAO for telescope time awarded through the Karl G. Jansky Very Large Array (VLA) interferometer for program Nos. 20B-280, 20A-469, 21B-176, and 21A-387. We also thank the NRAO staff for their help in the preparation of observations.

The Dunlap Institute is funded through an endowment established by the David Dunlap family and the University of Toronto.

Some of this work is based on observations obtained at the Gemini Observatory, which is operated by the Association of Universities for Research in Astronomy, Inc., under a cooperative agreement with the NSF on behalf of the Gemini partnership: the National Science Foundation (United States), the Science and Technology Facilities Council (United Kingdom), the National Research Council (Canada), CONICYT (Chile), the Australian Research Council (Australia), Ministério da Ciência e Tecnologia (Brazil), and SECYT (Argentina). We appreciate the Gemini team for granting us observing time for the program IDs: GN-2022A-Q-212, GN-2022B-Q-308, and GN-2022B-Q-116.

Basic research in radio astronomy at the U.S. Naval Research Laboratory is supported by 6.1 Base funding. The construction and installation of VLITE were supported by the NRL Sustainment Restoration and Maintenance fund.

B.M.G. acknowledges the support of the Natural Sciences and Engineering Research Council of Canada (NSERC) through grant RGPIN-2022-03163 and of the Canada Research Chairs program. M.R.D. acknowledges support from the NSERC through grant RGPIN-2019-06186, and of the Canada Research Chairs Program, and the Dunlap Institute at the University of Toronto. V.M.K. holds the Lorne Trottier Chair in Astrophysics & Cosmology, a Distinguished James McGill Professorship, and receives support from an NSERC Discovery grant (RGPIN-228738-13) and from the FRQNT CRAQ. J.W. T.H. is a Canada Excellence Research Chair in Transient Astrophysics.

N.S. acknowledges the support from NASA (grant No. 80NSSC22K0332), NASA FINESST (grant No. 80NSSC22K1597), Columbia University Dean's fellowship, and a grant from the Simons Foundation. T. E. is supported by

NASA through the NASA Hubble Fellowship grant HST-HF2-51504.001-A awarded by the Space Telescope Science Institute, which is operated by the Association of Universities for Research in Astronomy, Inc., for NASA, under contract NAS5-26555. A.M.C. is funded by an NSERC Doctoral Postgraduate Scholarship. A.B.P. is a Banting Fellow, a McGill Space Institute (MSI) Fellow, and a Fonds de Recherche du Quebec—Nature et Technologies (FRQNT) postdoctoral fellow. K.W.M. holds the Adam J. Burgasser Chair in Astrophysics and is supported by NSF grants (2008031, 2018490). S.P.T. is a CIFAR Azrieli Global Scholar in the Gravity and Extreme Universe Program. Z.P. was a Dunlap Fellow and is supported by an NWO Veni fellowship (VI. Veni.222.295). A.P. is funded by the NSERC Canada Graduate Scholarships—Doctoral program. K.N. is an MIT Kavli Fellow. F.K. acknowledges support from Onsala Space Observatory for the provisioning of its facilities/observational support. The Onsala Space Observatory national research infrastructure is funded through Swedish Research Council grant No. 2017-00648. M.B. is a McWilliams fellow and an International Astronomical Union Gruber fellow. M.B. also receives support from the McWilliams seed grant.

Facilities: CHIME, VLA, Gemini:Gillett.

Software: `FRUITBAT` (A. Batten 2019), `PHOTUTILS` (L. Bradley et al. 2023), `SExtractor` (E. Bertin & S. Arnouts 1996), `IRAF` (S. Blondin et al. 2012), `PYRAF` (Science Software Branch at STScI 2012), `PypeIt` (J. Prochaska et al. 2020), `CASA` (J. P. McMullin et al. 2007), `pwkit` (P. K. G. Williams et al. 2017), `AEGEAN` (P. J. Hancock et al. 2018), Astropy (Astropy Collaboration et al. 2013, 2018, 2022), Matplotlib (J. D. Hunter 2007), NumPy (C. R. Harris et al. 2020), SAOImage DS9 (W. A. Joye & E. Mandel 2003).

Appendix
Details of Individual Sources

Here, we provide an overview of each FRB field where a radio source was identified, detailing the relevant properties of the radio sources and their hosts. Table 7 presents the basic properties, while Table 8 displays the derived properties of each radio source.

Table 7
Summary of Archival, VLA, and VLITE Radio Results

FRB Name	Reference for FRB Region Used (90% cl)[o]	Radio Source	$S_{\nu,V}$[a] (mJy)	$S_{\nu,N}$[b] (mJy)	$S_{\nu,FI}$[c] (mJy)	$S_{\nu,L}$[d] (mJy)	R.A. (J2000)	Decl. (J2000)	$P_{cc,rad}$[e]	Nature[j]
FRB 20181030A	(1)	20181030A-S2[f]	<0.6	3.8 ± 0.5	<0.75	<0.42	10:34:22.74 (1.48 s)	+73:45:54.9(4.″5)	0.0954	R
FRB 20181119A	(2)	20181119A-S	<0.6	<12.5	<0.75	0.495 ± 0.095	12:41:51.72 (0.48 s)	+65:08:02.76 (0.″23)	0.7121	U
FRB 20190604A	(2)	20190604A-S1	<0.6	<12.5	<0.75	1.803 ± 0.188	14:34:48.86 (0.21 s)	+53:17:31.56 (0.″21)	0.2209	R
FRB 20190604A	(2)	20190604A-S2	<0.6	<12.5	<0.75	0.971 ± 0.175	14:34:48.97 (0.30 s)	+53:18:33.37 (0.″42)	0.4186	R
FRB 20190303A	(2)	20190303A-S1	<0.6	2.2 ± 0.4	<0.75	<0.42	13:51:59.91 (0.69 s)	+48:07:19.0(6.″9)	0.1673	E
FRB 20190303A	(2)	20190303A-S2	<0.6	<12.5	1.25 ± 0.13	<0.42	13:51:59.10	+48:07:29.3	0.2267	E
FRB 20190303A	(2)	20190303A-S3	<0.6	<12.5	<0.75	16.92 ± 0.39	13:51:59.518 (0.25 s)	+48:07:21.22 (0.″16)	⋯	B, E
FRB 20190110C	(3)	20190110C-S	0.77 ± 0.19	<12.5	0.91 ± 0.15	10.05 ± 0.29	16:37:17.84 (0.14 s)	+41:26:33.96 (0.″14)	0.0515[i]	U
FRB 20191106C	(3)	20191106C-S	<0.6	<12.5	<0.75	3.29 ± 0.14	13:18:19.22 (0.09 s)	+42:59:58.9 (0.″08)	0.1302	R
FRB 20191114A	(3)	20191114A-S	4.46 ± 0.26	9.1 ± 0.5	<0.75	<0.42	18:14:26.19 (0.06 s)	+19:47:48.3 (0.″03)	0.2913[g]	U
FRB 20200223B	(3)	20200223B-S	<0.6	<12.5	<0.75	2.964 ± 0.588	00:33:04.68 (1.22 s)	+28:49:52.5 (1.″17)	0.0863	E
FRB 20200619A	(3)	20200619A-S	1.89 ± 0.28	6.3 ± 0.5	<0.75	<0.42	18:10:17.37(0.1 s)	+55:37:15.1 (0.″12)	0.9065[h]	U
FRB 20200929C	(3)	20200929C-S	<0.6	<12.5	<0.75	1.705 ± 0.313	01:08:11.77 (0.27 s)	18:28:29.8(1.″4)	0.5516	R
			$S_{p,VLA}$[m] (mJy beam^{-1})	$S_{tot,VLA}$[n] (mJy)	$S_{p,VLITE}$[p] (mJy beam^{-1})	$S_{tot,VLITE}$[p] (mJy)				
FRB 20180814A	(2)	20180814A-S1	0.018 ± 0.003	0.0673 ± 0.0128	...	<1.6	04:22:56.11 (0.23 s)	+73:39:40.3 (0.30″)	0.5162	E
FRB 20180814A	(2)	20180814A-S2	0.020 ± 0.004	0.0197 ± 0.0038	...	<1.6	04:22:51.82 (0.15 s)	+73:39:53.68 (0.15″)	0.0192	U
FRB 20180814A	(2)	20180814A-S3	0.022 ± 0.004	0.026 ± 0.0044	...	<1.6	04:22:38.8(0.15 s)	+73:40:15.21 (0.14″)	0.0129	U
FRB 20180814A	(2)	20180814A-S4	0.029 ± 0.003	0.065 ± 0.007	...	<1.6	04:22:41.3(0.14 s)	+73:40:21.04 (0.12″)	⋯	E
FRB 20180814A	(2)	20180814A-S5	0.033 ± 0.002	0.20 ± 0.01	...	<1.6	04:22:46.3(0.13 s)	+73:40:20.41 (0.13″)	⋯	E
FRB 20181030A	(1)	20181030A-S1	0.40 ± 0.02	0.43 ± 0.02	...	<2.2	10:34:14.25 (0.02 s)	+73:45:04.1 (0.02″)	0.3718	U
FRB 20190208A	(2)	20190208A-S	0.07 ± 0.02	0.0791 ± 0.0055	...	<1.7	18:54:07.11 (0.05 s)	+46:55:51.9 (0.03″)	0.8217	U
FRB 20190117A	(2)	20190117A-S	0.18 ± 0.02	0.2078 ± 0.0194	...	<4.8	22:06:36.95 (0.15 s)	+17:22:25.7 (0.08″)	0.6982	U
FRB 20190303A	(2)	20190303A-S1[k]	0.06	0.2677	1.4 ± 0.3	7.7 ± 1.9	13:51:59.9	+48:07:17.55	0.6521	E
FRB 20190303A	(2)	20190303A-S2[l]	0.07	0.9516	1.9 ± 0.3	10.0 ± 2.1			0.2700	E

Table 7
(Continued)

FRB Name	Reference for FRB Region Used (90% cl)[o]	Radio Source	$S_{\nu,V}$[a] (mJy)	$S_{\nu,N}$[b] (mJy)	$S_{\nu,F}$[c] (mJy)	$S_{\nu,L}$[d] (mJy)	R.A. (J2000)	Decl. (J2000)	$P_{cc,rad}$[e]	Nature[j]
							13:51:59.01 (0.02 s)	+48:07:24.3 (0.02″)		
FRB 20190417A	(2)	20190417A-S1	0.164 ± 0.008	0.1727 ± 0.0089	...	<1.1	19:39:05.89 (0.03 s)	+59:19:36.8 (0.03″)	0.6705	U
FRB 20190417A	(2)	20190417A-S2	0.043 ± 0.008	0.057 ± 0.012	...	<1.1	19:39:00.44 (0.18 s)	+59:20:02.4 (0.12″)	0.9914	R

Notes. This table contains all radio (archival and targeted VLA) sources including extended and blended ones. The topmost set is archival data followed by the VLA data after the dividing line and all upper limits quoted for each survey are the 5σ rms value.

[a] V means VLASS.

[b] N means NVSS.

[c] F means FIRST.

[d] L means LoTSS.

[e] $P_{cc,rad}$ is the probability of finding a radio flux as bright as S_ν within each FRB error region (see Section 2.6).

[f] Flux density values and other information related to this source are taken from M. Bhardwaj et al. (2021b).

[g] The $P_{cc,rad}$ value shown in the table is for VLASS. $P_{cc,rad}$ for the NVSS source is 0.7154. There is also radio emission at the location of 20191114A-S from RACS with a flux density of 15.49 ± 0.72 mJy at $P_{cc,rad}$ of 0.2347 and emission from TGSS with a flux density of 33.9 ± 6.3 mJy at $P_{cc,rad}$ of 0.3181.

[h] The $P_{cc,rad}$ value shown in the table is for VLASS. The $P_{cc,rad}$ for NVSS is 0.7707. There is also a TGSS source at the location of 20200619A-S with a flux density of 28.6 ± 5.6 mJy at $P_{cc,rad}$ of 0.785.

[i] The $P_{cc,rad}$ value shown in the table is for the VLASS source. The $P_{cc,rad}$ value is 0.1012 for the FIRST source while the LoTSS source is blended.

[j] Nature here refers to the size of the radio source. U means that the radio source is unresolved, R means that the source is resolved (radio source size is more than the beam size), B means that the source is blended with another radio source, and E means that the radio source is extended (see Section 4.1 for details.). We refrained from computing $P_{cc,rad}$ values for the blended sources due to the ambiguity in determining their flux densities.

[k] This VLA source is multicomponent but at the location of the NVSS source.

[l] This VLA source is at the location of the FIRST source.

[m] $S_{p,VLA}$ is the peak flux density for the VLA source.

[n] $S_{tot,VLA}$ is the integrated flux density for the VLA source.

[o] cl means confidence level. (1) M. Bhardwaj et al. (2021b), (2) D. Michilli et al. (2023), and (3) CHIME/FRB Collaboration & B. C. Andersen (2023).

[p] Peak and integrated fluxes and limits from VLITE (0.34 GHz). The limits are 5σ upper limits used to constrain the spectral indices of the VLA sources.

Table 8
Derived Properties of the Radio Sources

Radio Source	z_{max}	z_{spec}	$L_{\nu,V}$ ($\times 10^{30}$)	$L_{\nu,N}$ ($\times 10^{30}$)	$L_{\nu,F}$ ($\times 10^{30}$)	$L_{\nu,L}$ ($\times 10^{30}$)	$L_{\nu,VLA}$[l] ($\times 10^{28}$)	α_{in}[a]	α[a]	Host[f]
					(erg s^{-1} Hz^{-1})					
20181030A-S2[b]	<0.05[b]	0.00385[b]	<0.0002	1.57(27)	<0.0003	<0.0001	⋯	...	> -0.43	Y, E
20181119A-S	<0.43[c]	⋯	<4.27	<89.01	<5.34	3.526	⋯	...	< -0.063	N
20190604A-S1	<0.7[c]	⋯	<13.80	<287.57	<17.25	41.48	⋯	...	< -0.359	N
20190604A-S2	<0.7[c]	⋯	<13.80	<287.57	<17.25	22.33	⋯	...	< -0.157	Y, E
20190303A-S1	<0.22[c]	0.06437(1)[c]	<0.063	0.24(4)	⋯	⋯	⋯	...	< -1.70	Y, E
20190303A-S2	<0.22[c]	0.06386(1)[c]	<0.063	⋯	0.13(1)	⋯	⋯	...	< -0.96	Y, E
20190303A-S3	<0.22[c]	0.06386(1)[c,d]	<0.063	⋯	⋯	1.78(4)	⋯	...	< -1.09	Y, E
20190110C-S	<0.22[e]	⋯	1.17	<1.89	1.38	15.25[l]	⋯	...	$-0.09(1)$[h]	Y, E
20191106C-S	<0.36[e]	0.10775(1)[e]	<0.19	<3.97	<0.24	1.05(4)	⋯	...	< -0.55	Y, E
20191114A-S	<0.52	⋯	49.80	101.64	<8.40	<4.71	⋯	...	$-2.9(4)$[g]	N
20200223B-S	<0.19[e]	0.06024(2)[e]	<0.056	<1.164	<0.069	0.28(5)	⋯	...	< -0.52	Y, E
20200619A-S	<0.45	⋯	14.97	49.97	5.95	3.332	⋯	...	$-2.8(4)$[g]	Y, U
20200929C-S	<0.44	⋯	<4.513	<94.03	<5.641	12.83	⋯	...	< -0.34	Y, E
20180814A-S1	<0.091[c]	0.06835(1)[c]	...	...	...	...	0.82(15)	$-1.8(1.2)$	> -3.02[i]	Y, E
20180814A-S2	<0.091[c]	⋯	...	...	...	...	0.44(8)	$-2.7(1.1)$	> -2.95[i]	N
20180814A-S3	<0.091[c]	⋯	...	...	...	...	0.58(9)	$-1.3(9)$	> -2.88[i]	N
20180814A-S4	<0.091[c]	0.376(1)[c]	...	...	...	...	1.44(16)	0.1(6)	> -2.70[i]	Y, E
20180814A-S5	<0.091[c]	0.237(1)[c]	...	...	...	...	4.43(22)	0.2(6)	> -2.61[i]	Y, E
20181030A-S1	<0.05[b]	0.00385(2)[b]	...	...	...	...	0.02(1)	$-0.77(2)$	> -1.13[i]	Y, E
20190208A-S	<0.68[c]	⋯	...	...	...	...	16.9(1.2)	$-1.3(5)$	> -2.15[i]	Y, U
20190117A-S	<0.46[c]	⋯	...	...	...	...	174(16)	$-0.8(6)$	> -2.21[i]	A[j]
20190303A-S1	<0.22[c]	0.06437(1)[c]	...	...	...	...	2.86[m]	⋯	-1.1 ± 0.3[i]	Y, E
20190303A-S2	<0.22[c]	0.063861(1)[c]	...	...	...	...	0.1[m]	⋯	-1.6 ± 0.3[i]	Y, E
20190417A-S1	<1.2[c]	0.12817(2)	...	...	...	...	7.97(41)	$-1.2(4)$	> -1.25[i]	A[k]
20190417A-S2	<1.2[c]	⋯	...	...	...	...	493(104)	$-4.2(1.4)$	> -2.15[i]	N

Notes. The table comprises properties of all radio sources obtained from archival and targeted VLA observations. Luminosities were calculated utilizing the available z_{spec} (spectroscopic redshift) or z_{max} (maximum redshift) in cases where z_{spec} is unavailable. Luminosities derived from z_{spec} are treated as absolute values, whereas those derived from z_{max} serve as upper limits within the FRB framework. In instances of nondetections, the symbol < denotes upper limits. V means VLASS at 3 GHz, N means NVSS at 1.4 GHz, F means FIRST at 1.4 GHz, L means LoTSS at 0.14 GHz.

[a] The spectral index (α) characterizes the radio source based on flux densities obtained from at least two frequencies, while α_{in} is the in-band spectral index, ($\alpha = I_1/I_0$) (see Section 4.3 for details). Upper and lower limit values of α were determined utilizing VLASS nondetection data and detections of each individual radio source.

[b] Values taken from M. Bhardwaj et al. (2021b).

[c] Values taken from D. Michilli et al. (2023).

[d] Two merging galaxies have been reported as the host of FRB 20190303A. The LoTSS source associated with this FRB is in between the two merging galaxies, so we adopted the galaxy redshift of $z = 0.064(1)$ for estimating its luminosity.

[e] Values are taken from A. L. Ibik et al. (2024).

[f] Y means yes, there is an optical source that is likely the host galaxy associated with the radio source; E means that there is an extended optical source at the position of the radio source; U means that the optical source at the position of the radio source is unresolved; R means that the optical source at the position of the radio source is resolved; and N means no, there is no optical source that is likely a host galaxy of the radio source.

[g] These spectral indices were estimated using the VLASS and the NVSS sources.

[h] The spectral index for this source was calculated using the VLASS and the FIRST sources.

[i] Contemporaneous spectral index taken from VLITE (0.34 GHz) and VLA (1.5 GHz).

[j] This source is classified by DESI to be a point source with a very low probability of being a star. This may be an unresolved galaxy.

[k] This source was not detected in any archival catalog but was found using targeted Gemini observation in "*grz*" bands (see Section A.9 for details). This source is classified as unresolved.

[l] $L_{\nu,VLA}$ is obtained using the integrated flux density of each VLA source.

[m] The source finder could not find flux density errors for these sources.

A.1. FRB 20180814A Field

FRB 20180814A is part of the first set of repeating FRBs to be discovered by CHIME/FRB and has a DM of 189.4(4) pc cm^{-3} (D. Michilli et al. 2023). We used the baseband localization region and $z_{max} = 0.091$ published by D. Michilli et al. (2023) to search for radio sources in its field.

We conducted an archival search for radio sources in the field of FRB 20180814A but found none. However, we found five radio sources from the VLA deep image at 1.5 GHz of the field. Out of the five radio sources, two (20180814A-S2 and 20180814A-S3) could not be associated with a galaxy while another two (20180814A-S4 and 20180814A-S5) have likely host-galaxy associations.

One of the VLA radio sources (20180814A-S1) found in this field is extended and spatially coincident with the plausible host galaxy of the FRB. 20180814A-S2 and 20180814A-S3 are unresolved sources and thus likely PRS candidates. However, 20180814A-S1, 20180814A-S4, and 20180814A-S5 are

extended radio sources; thus, we disfavor them as potential PRSs.

The likely host galaxy of the 20180814A-S1 is the same as the plausible host of the FRB, which was discovered from the PanSTARRS survey to be PanSTARRS-DR1 J042256.01 +733940.7 at a $z_{\rm spec} = 0.06835(1)$ with an AB apparent magnitude of 17.15 mag, as reported by D. Michilli et al. (2023).

In the case where the FRB is not associated with any radio source, we take the 5σ rms value of 17.5 μJy as the upper limit on the flux density of the PRS at 1.5 GHz.

A.2. FRB 20180916B Field

FRB 20180916B is a well-studied repeating FRB source. Its relatively close proximity of approximately 150 Mpc despite having a DM of 348.77 pc cm^{-3} (CHIME/FRB Collaboration et al. 2020), combined with thorough investigations into the bursts, has unveiled valuable insights into its characteristics — notably, the presence of a 16.3 day periodicity in its activity (Z. Pleunis et al. 2021). B. Marcote et al. (2020) achieved a subarcsecond localization of the source using VLBI with the European VLBI Network (EVN), linking the FRB to a star-forming region within a massive spiral galaxy at a redshift of 0.0337.

There have not been any radio sources found at the location of the FRB after various efforts (B. Marcote et al. 2020). Here, we report a similar deep limit on the presence of a PRS at the location of the FRB using our realfast/VLA image of the field (see Figure 2). We measure an upper limit on flux density above a 3σ rms noise level of 18 μJy beam^{-1} at 1.5 GHz. This resulted in an upper limit on PRS luminosity of $<4.8 \times 10^{26}$ erg s^{-1} Hz^{-1}, which is the same as the earlier constraint provided by B. Marcote et al. (2020).

A.3. FRB 20181030A Field

FRB 20181030A is a repeater that is prominent for coming from a large, nearby bright galaxy. It was reported to have a DM of 103.5 pc cm^{-3}, which is approximately 20 Mpc away according to M. Bhardwaj et al. (2021b). The plausible host of FRB 20181030A is a large spiral galaxy known as NGC 3252 ($z = 0.00385$) with an NVSS (NVSS J103422+734554) radio source close to the center of the galaxy reported by M. Bhardwaj et al. (2021b) and a VLA source—20181030A-S1 seen at the edge as described here. Considering the offset, lack of WISE emission, and star formation information, we consider 20181030A-S1 a candidate PRS even though we are unable to rule out background AGN.

In the case where the FRB is not associated with any radio source, we take the 5σ rms value of 50 μJy as the upper limit on the flux density of the PRS at 1.5 GHz. This results in an upper limit on luminosity of $<2.4 \times 10^{25}$ erg s^{-1} Hz^{-1}.

A.4. FRB 20181119A Field

FRB 20181119A is one of the second set of repeaters discovered by CHIME/FRB with a $z_{\rm max}$ of 0.43 (CHIME/FRB Collaboration & B. C. Andersen 2023). The radio source (ILTJ124151.73+650802.7, hereafter 20181119A-S) was found in the LoTSS survey but did not have an optical host association. This is the only source in our sample with a positive spectral index limit similar to that found for a third potential PRS—FRB 20201124A (G. Bruni et al. 2024).

Additionally, there appears to be a probable second LoTSS source located at another edge of this FRB field, yet it was not documented in the LoTSS catalog.

A.5. FRB 20190110C Field

FRB 20190110C is a part of the third set of repeating FRBs discovered by CHIME/FRB with $z_{\rm max} = 0.22$ (CHIME/FRB Collaboration & B. C. Andersen 2023). There is a 92% likelihood (as estimated by the Probabilistic Association of Transients to their Hosts, hereafter PATH, software) of the FRB being linked to a galaxy at $z_{\rm spec} = 0.12244(6)$ (A. L. Ibik et al. 2024). Initial archival searches within the uncertainty region revealed a radio source (20190110C-S) in various catalogs, including VLASS, FIRST, and LoTSS as shown in Table 7.

The radio source is likely associated with a faint galaxy close to the PATH-preferred FRB host. Since PATH does not necessarily exclude other galaxies in the field, we investigate the galaxy further. We found a single line $z_{\rm spec} > z_{\rm max}$, and this rules out this source. Even if we think this redshift is incorrect, the offset, RO ratio, and WISE color ratios are consistent with AGN.

A.6. FRB 20190117A Field

FRB 20190117A belongs to the second set of repeating FRBs to be discovered by CHIME/FRB. We used the baseband localization region, and $z_{\rm max} = 0.46$ published by D. Michilli et al. (2023) to search for radio sources in its field. No radio source was detected in an initial archival search within the localization uncertainty region of the burst, but we found a VLA source (20190117A-S) just outside the field. The radio source is likely associated with an unresolved optical counterpart with a small offset consistent with AGN. In the case where the FRB is not associated with any radio source, we take the 5σ rms value of 80 μJy as the upper limit on the flux density of the PRS at 1.5 GHz.

A.7. FRB 20190208A Field

FRB 20190208A is part of the second set of repeating FRBs to be discovered by CHIME/FRB. We used the baseband localization region, and $z_{\rm max} = 0.68$ published by D. Michilli et al. (2023) to search for radio sources in its field. No radio source was detected in an initial archival search within the localization uncertainty region of the burst, but we found a VLA source (20190208A-S) just outside the field. The radio source is likely associated with an unresolved optical counterpart with a small offset consistent with AGN.

In the case where the FRB is not associated with any radio source, we take the 5σ rms value of 25 μJy as the upper limit on the flux density of the PRS at 1.5 GHz.

A.8. FRB 20190303A Field

FRB 20190303A is among the second set of repeating FRBs whose baseband localizations were published by D. Michilli et al. (2023), with $z_{\rm max} = 0.22$. The plausible host of FRB 20190303A is two merging galaxies known as SDSS J135159.17+480729.0 and SDSS J135159.87+480714.2 with $z_{\rm spec} = 0.06437(1)$ and $z_{\rm spec} = 0.06386(1)$ respectively as reported by D. Michilli et al. (2023). We discovered an NVSS radio source spatially coincident with SDSS J135159.17

+480729.0 ($P_{\rm cc,rad} \sim 0.1673$), an FIRST source spatially coincident with SDSS J135159.87+480714.2 ($P_{\rm cc,rad} \sim 0.2268$), and an LoTSS source overlapping the two galaxies ($P_{\rm cc,rad} \sim 0.1283$).

Since the LoTSS radio source is quite offset from both galaxies, we know that it is not an AGN, but its blended nature makes it ambiguous, and thus, we are unable to associate it with any of the galaxies. A deeper observation of the field revealed two distinct extended radio sources (20190303A-S1 and 20190303A-S2) that nicely traced the shape of the two merging galaxies. However, we are not able to detangle any point source even if embedded in the radio source; hence, we report the measured radio emissions and upper limits. The morphology of these emissions is consistent with star formation activities of their host galaxies or probably a consequence of the merging of the two galaxies; hence, they are ruled out as PRSs.

In the case where the FRB is not associated with any radio source, we take the 5σ rms value of 25 μJy as the upper limit on the flux density of the PRS at 1.5 GHz. This gives a radio luminosity of $<2.6 \times 10^{27}$ erg s^{-1} Hz^{-1} for the FRB.

A.9. FRB 20190417A Field

FRB 20190417A is one of the very high DM repeating FRBs reported by CHIME/FRB among the second set of repeaters. We used the baseband localization region, and $z_{\rm max} = 1.2$ published by D. Michilli et al. (2023) to search for radio sources in its field. No radio source was detected in an initial archival search within the localization uncertainty region of the burst.

VLA imaging of the FRB localization uncertainty region showed two radio sources in the field. The first source (20190417A-S1) is likely a PRS when considered in the context of its optical host ($z_{\rm spec} = 0.12817(2)$) imaged with Gemini North.

Using the line fluxes from Gemini North spectra, we construct and place this galaxy on the updated BPT (J. A. Baldwin et al. 1981) diagram according to L. Trouille et al. (2011). The line ratio location is consistent with a star-forming galaxy. Using the extinction-corrected spectra, we estimate the H_α luminosity to be 3.7×10^{40} erg s^{-1}. In addition, we also check for intrinsic host-galaxy extinction by calculating the Balmer decrement from the H_α and H_β line fluxes. Compared to the theoretical Case-B recombination line ratio of $H_\alpha/H_\beta = -3.3$, we do not find evidence for significant additional extinction given that we measure a Balmer decrement of 1.76. We then calculate the $\rm SFR_{H_\alpha}$ to be $0.1964\, M_\odot\, {\rm yr}^{-1}$ as described in Section 4.8. We estimate a metallicity of $12 + \log({\rm O/H}) = 8.91$ using Equation (1) from M. Pettini & B. E. J. Pagel (2004): $12 + \log({\rm O/H}) = 8.90 + 0.57\times$ N2, where N2 = [N II]λ6583/H_α. This value is approximately similar to solar metallicity assuming $12 + \log({\rm O/H})_{\rm solar} = 8.69$. All these results insinuate that this unresolved optical source is a star-forming galaxy. Considering the physical offset, lack of WISE emission, and star formation information, we consider 20190417A-S1 a potential PRS. The second source (20190417A-S2) is resolved and has no optical counterpart.

In the case where the FRB is not associated with any radio source, we take the 5σ rms value of 42.5 μJy as the upper limit on the flux density of the PRS at 1.5 GHz.

A.10. FRB 20190604A Field

FRB 20190604A is part of the second set of repeating CHIME/FRBs whose baseband localizations were published by D. Michilli et al. (2023), and has $z_{\rm max} = 0.7$ from its DM. In the field of FRB 20190604A, there are two resolved LoTSS sources; ILTJ143448.87+531731.2 (20190604A-S1) and ILTJ143448.97+531833.3 (20190604A-S2).

Since these two radio sources are resolved, we did not discuss them further in the context of this study.

A.11. FRB 20191106C Field

FRB 20191106C is one of the third set of repeaters discovered by CHIME/FRB with a $z_{\rm max} = 0.36$ (CHIME/FRB Collaboration & B. C. Andersen 2023; A. L. Ibik et al. 2024). We found an LoTSS source (ILTJ131819.22+425958.9, hereafter 20191106C-S) spatially associated with the plausible host of the FRB with $z_{\rm spec} = 0.10775(1)$ as reported by A. L. Ibik et al. (2024) at an offset of 0.″11 from the center of the galaxy. The radio source is resolved and is likely consistent with AGN given the offset.

A.12. FRB 20191114A Field

FRB 20191114A is among the third set of FRB repeaters discovered and positions published by CHIME/FRB with a $z_{\rm max}$ of 0.52 (CHIME/FRB Collaboration & B. C. Andersen 2023). We found an NVSS (NVSS J181426+194749), TGSS (J181426.2+194749), and RACS (RACS 1819+18A) radio source at the edge of the FRB region. A VLASS source (VLASS1QLCIR J181426.18+194748.2) was found at the same location but offset from the FRB region and referred to as 20191114A-S. There is no optical host association for the radio source; hence, we could not characterize the source further.

A.13. FRB 20200120E Field

FRB 20200120E is the only repeating FRB that is associated with a globular cluster in the M81 spiral galaxy (M. Bhardwaj et al. 2021a; F. Kirsten et al. 2022). Its low DM of 87.82 pc cm^{-3} (M. Bhardwaj et al. 2021a) is consistent with the distance to M81 of 3.6 Mpc. F. Kirsten et al. (2022) reported a VLBI localization of the source with the EVN. To date, no coincident radio sources have been identified at this location. Here, we present an upper limit on the presence of a PRS at the FRB's location using a realfast/VLA image of the field (see Figure 2). Our analysis yields an upper limit on the flux density, exceeding a 3σ rms noise level of 27 μJy beam^{-1} at 1.5 GHz. Consequently, we establish an upper limit on the PRS luminosity of $<4.2 \times 10^{23}$ erg s^{-1} Hz^{-1}, which is slightly higher by an order of magnitude than the earlier constraint provided by F. Kirsten et al. (2022).

A.14. FRB 20200223B Field

FRB 20200223B is one of the third set of repeaters discovered by CHIME/FRB with a DM of 201.8(4) pc cm^{-3} corresponding to a $z_{\rm max} = 0.19$ (CHIME/FRB Collaboration & B. C. Andersen 2023; A. L. Ibik et al. 2024). We found an extended LoTSS source (ILTJ003304.67+284952.4) in the field of FRB 20200223B, spatially associated with the plausible host of the FRB ($z_{\rm spec} = 0.06024(2)$) at an offset of 0′.17 as reported by A. L. Ibik et al. (2024).

A.15. FRB 20200619A Field

FRB 20200619A is one of the third set of repeaters discovered by CHIME/FRB with a $z_{\max} = 0.45$ (CHIME/FRB Collaboration & B. C. Andersen 2023). An archival search of the localization region revealed an NVSS (NVSS J181016+553724) and a TGSS ADR1 (J181015.3+553736) source at the edge of the CHIME error region for the FRB. The source looks like three individual sources in the VLASS image. However, the source catalog only identified the one close to the center of the emission VLASS1QLCIR J181017.37+553715.0 (which is a bit outside the FRB field). The radio source is likely associated with an unresolved optical galaxy.

A.16. FRB 20200929C Field

FRB 20200929C is a repeating FRB identified by CHIME/FRB among the third set of repeaters with a $z_{\max}$ of 0.44 (CHIME/FRB Collaboration & B. C. Andersen 2023). We found an LoTSS source (ILTJ010811.77+182829.7) within the error region.

While we still do not know the host galaxy of the FRB, the radio source is spatially coincident with an SDSS galaxy (SDSSJ010811.69+182830.8) at $z_{\rm ph} = 0.40 \pm 0.09$.

ORCID iDs

Adaeze L. Ibik https://orcid.org/0000-0003-2405-2967
Maria R. Drout https://orcid.org/0000-0001-7081-0082
B. M. Gaensler https://orcid.org/0000-0002-3382-9558
Paul Scholz https://orcid.org/0000-0002-7374-7119
Navin Sridhar https://orcid.org/0000-0002-5519-9550
Ben Margalit https://orcid.org/0000-0001-8405-2649
T. E. Clarke https://orcid.org/0000-0001-6812-7938
Casey J. Law https://orcid.org/0000-0002-4119-9963
Shriharsh P. Tendulkar https://orcid.org/0000-0003-2548-2926
Daniele Michilli https://orcid.org/0000-0002-2551-7554
Tarraneh Eftekhari https://orcid.org/0000-0003-0307-9984
Mohit Bhardwaj https://orcid.org/0000-0002-3615-3514
Sarah Burke-Spolaor https://orcid.org/0000-0003-4052-7838
Shami Chatterjee https://orcid.org/0000-0002-2878-1502
Amanda M. Cook https://orcid.org/0000-0001-6422-8125
Jason W. T. Hessels https://orcid.org/0000-0003-2317-1446
Franz Kirsten https://orcid.org/0000-0001-6664-8668
Ronniy C. Joseph https://orcid.org/0000-0003-3457-4670
Victoria M. Kaspi https://orcid.org/0000-0001-9345-0307
Mattias Lazda https://orcid.org/0000-0002-5857-4264
Kiyoshi W. Masui https://orcid.org/0000-0002-4279-6946
Kenzie Nimmo https://orcid.org/0000-0003-0510-0740
Ayush Pandhi https://orcid.org/0000-0002-8897-1973
Aaron B. Pearlman https://orcid.org/0000-0002-8912-0732
Ziggy Pleunis https://orcid.org/0000-0002-4795-697X
Masoud Rafiei-Ravandi https://orcid.org/0000-0001-7694-6650
Kaitlyn Shin https://orcid.org/0000-0002-6823-2073
Kendrick M. Smith https://orcid.org/0000-0002-2088-3125

References

Afonso, J., Georgakakis, A., Almeida, C., et al. 2005, ApJ, 624, 135
Ahn, C. P., Alexandroff, R., Allende Prieto, C., et al. 2012, ApJS, 203, 21
Alexander, K. D., Laskar, T., Berger, E., et al. 2017, ApJ, 848, 69
Andreoni, I., Lu, W., Smith, R. M., et al. 2020, ApJL, 896, L2
Astropy Collaboration, Price-Whelan, A. M., Lim, P. L., et al. 2022, ApJ, 935, 167
Astropy Collaboration, Price-Whelan, A. M., Sipőcz, B. M., et al. 2018, AJ, 156, 123
Astropy Collaboration, Robitaille, T. P., Tollerud, E. J., et al. 2013, A&A, 558, A33
Baldwin, J. A., Phillips, M. M., & Terlevich, R. 1981, PASP, 93, 5
Batten, A. 2019, JOSS, 4, 1399
Becker, R. H., White, R. L., & Helfand, D. J. 1995, ApJ, 450, 559
Beloborodov, A. M. 2017, ApJL, 843, L26
Berger, E., Kulkarni, S. R., Pooley, G., et al. 2003, Natur, 426, 154
Bertin, E., & Arnouts, S. 1996, A&AS, 117, 393
Bhandari, S., Gordon, A. C., Scott, D. R., et al. 2023a, ApJ, 948, 67
Bhandari, S., Marcote, B., Sridhar, N., et al. 2023b, ApJL, 958, L19
Bhardwaj, M., Gaensler, B. M., Kaspi, V. M., et al. 2021a, ApJL, 910, L18
Bhardwaj, M., Kirichenko, A. Y., Michilli, D., et al. 2021b, ApJL, 919, L24
Blondin, S., Matheson, T., Kirshner, R. P., et al. 2012, AJ, 143, 126
Bloom, J. S., Kulkarni, S. R., & Djorgovski, S. G. 2002, AJ, 123, 1111
Bochenek, C. D., Ravi, V., Belov, K. V., et al. 2020, Natur, 587, 59
Bradley, L., Sipőcz, B., Robitaille, T., et al. 2023, astropy/photutils: v1.8.0, Zenodo, doi:10.5281/zenodo.7946442
Bruni, G., Piro, L., Yang, Y.-P., et al. 2024, Natur, 632, 1014
Cardelli, J. A., Clayton, G. C., & Mathis, J. S. 1989, ApJ, 345, 245
Cassanelli, T., Leung, C., Rahman, M., et al. 2022, AJ, 163, 65
Cenko, S. B., Frail, D. A., Harrison, F. A., et al. 2010, ApJ, 711, 641
Chambers, K. C., Magnier, E., Metcalfe, N., et al. 2016, arXiv:1612.05560
Chatterjee, S., Law, C. J., Wharton, R. S., et al. 2017, Natur, 541, 58
Chen, G., Ravi, V., & Hallinan, G. W. 2023, ApJ, 958, 185
Chevalier, R. A. 1998, ApJ, 499, 810
Chevalier, R. A., & Fransson, C. 2006, ApJ, 651, 381
Chibueze, J. O., Caleb, M., Spitler, L., et al. 2022, MNRAS, 515, 1365
CHIME/FRB Collaboration, Amiri, M., Andersen, B. C., et al. 2021, ApJS, 257, 59
CHIME/FRB Collaboration, Andersen, B. C. 2023, ApJ, 947, 83
CHIME/FRB Collaboration, Andersen, B. C., Bandura, K., et al. 2019, ApJL, 885, L24
CHIME/FRB Collaboration, Andersen, B. C., Bandura, K., et al. 2020, Natur, 587, 54
Clarke, T. E., Kassim, N. E., Brisken, W., et al. 2016, Proc. SPIE, 9906, 99065B
Condon, J. J., Cotton, W. D., Greisen, E. W., et al. 1998, AJ, 115, 1693
Cordes, J. M., & Lazio, T. J. W. . 2002, arXiv:astro-ph/0207156
Cotton, W. D. 2008, PASP, 120, 439
Crowther, P. A. 2013, MNRAS, 428, 1927
Deller, A. T., Tingay, S. J., Bailes, M., & West, C. 2007, PASP, 119, 318
Dey, A., Schlegel, D. J., Lang, D., et al. 2019, AJ, 157, 168
Dong, Y., Eftekhari, T., Fong, W., et al. 2024b, ApJ, 973, 133
Dong, Y., Eftekhari, T., Fong, W.-f., et al. 2024a, ApJ, 961, 44
Driver, S. P., Andrews, S. K., Davies, L. J., et al. 2016a, ApJ, 827, 108
Driver, S. P., Wright, A. H., Andrews, S. K., et al. 2016b, MNRAS, 455, 3911
Eftekhari, T., & Berger, E. 2017, ApJ, 849, 162
Eftekhari, T., Berger, E., Margalit, B., et al. 2019, ApJL, 876, L10
Eftekhari, T., Berger, E., Williams, P. K. G., & Blanchard, P. K. 2018, ApJ, 860, 73
Eftekhari, T., Margalit, B., Omand, C. M. B., et al. 2021, ApJ, 912, 21
Feng, Y., Li, D., Yang, Y.-P., et al. 2022, Sci, 375, 1266
Fonseca, E., Andersen, B. C., Bhardwaj, M., et al. 2020, ApJL, 891, L6
Frail, D. A., Soderberg, A. M., Kulkarni, S. R., et al. 2005, ApJ, 619, 994
Gehrels, N. 1986, ApJ, 303, 336
Goeman, J. J., & Solari, A. 2014, Statistics in Medicine, 33, 1946
Gordon, Y. A., Boyce, M. M., O'Dea, C. P., et al. 2021, ApJS, 255, 30
Greisen, E. W. 2003, in Astrophysics and Space Science Library, Information Handling in Astronomy—Historical Vistas, ed. A. Heck, Vol. 285 (Dordrecht: Kluwer), 109
Hancock, P. J., Murphy, T., Gaensler, B. M., Hopkins, A., & Curran, J. R. 2012, MNRAS, 422, 1812
Hancock, P. J., Trott, C. M., & Hurley-Walker, N. 2018, PASA, 35, e011
Harris, C. R., Millman, K. J., van der Walt, S. J., et al. 2020, Natur, 585, 357
Hook, I. M., Jørgensen, I., Allington-Smith, J. R., et al. 2004, PASP, 116, 425
Hunter, J. D. 2007, CSE, 9, 90
Ibik, A. L., Drout, M. R., Gaensler, B. M., et al. 2024, ApJ, 961, 99
Ibik, A. L., Drout, M. R., Margutti, R., et al. 2024, ApJ, submitted
Intema, H. T., Jagannathan, P., Mooley, K. P., & Frail, D. A. 2017, A&A, 598, A78
Jarrett, T. H., Cluver, M. E., Magoulas, C., et al. 2017, ApJ, 836, 182

Joye, W. A., & Mandel, E. 2003, in ASP Conf. Ser. 295, Astronomical Data Analysis Software and Systems XII, ed. H. E. Payne, R. I. Jedrzejewski, & R. N. Hook (San Francisco, CA: ASP), 489
Kilpatrick, C. D., Burchett, J. N., Jones, D. O., et al. 2021, ApJ, 907, L3
Kirsten, F., Marcote, B., Nimmo, K., et al. 2022, Natur, 602, 585
Kirsten, F., Snelders, M. P., Jenkins, M., et al. 2020, NatAs, 5, 414
Kumar, P., Beniamini, P., Gupta, O., & Cordes, J. M. 2024, MNRAS, 527, 457
Kumar, P., & Bošnjak, Ž. 2020, MNRAS, 494, 2385
Kumar, P., Lu, W., & Bhattacharya, M. 2017, MNRAS, 468, 2726
Lacy, M., Baum, S. A., Chandler, C. J., et al. 2020, PASP, 132, 035001
Lanman, A. E., Andrew, S., Lazda, M., et al. 2024, AJ, 168, 87
Laskar, T., van Eerten, H., Schady, P., et al. 2019, ApJ, 884, 121
Law, C. J., Bower, G. C., Burke-Spolaor, S., et al. 2018, ApJS, 236, 8
Law, C. J., Connor, L., & Aggarwal, K. 2022, ApJ, 927, 55
Leung, C., Mena-Parra, J., Masui, K., et al. 2021, AJ, 161, 81
Li, Q.-C., Yang, Y.-P., & Dai, Z.-G. 2020, ApJ, 896, 71
Lin, H.-H., Lin, K.-y., Li, C.-T., et al. 2022, PASP, 134, 094106
Lorimer, D. R., Bailes, M., McLaughlin, M. A., Narkevic, D. J., & Crawford, F. 2007, Sci, 318, 777
Lorimer, D. R., & Kramer, M. 2004, Handbook of Pulsar Astronomy, 4 (Cambridge: Cambridge Univ. Press)
Machalski, J., & Condon, J. J. 1999, ApJS, 123, 41
Macquart, J.-P., Prochaska, J. X., McQuinn, M., et al. 2020, Natur, 581, 391
Malesani, D., Fynbo, J. P. U., Hjorth, J., et al. 2009, ApJL, 692, L84
Marcote, B., Nimmo, K., Hessels, J. W. T., et al. 2020, Natur, 577, 190
Marcote, B., Nimmo, K., Salafia, O. S., et al. 2019, ApJ, 876, L14
Marcote, B., Paragi, Z., Hessels, J. W. T., et al. 2017, ApJL, 834, L8
Margalit, B., Berger, E., & Metzger, B. D. 2019, ApJ, 886, 110
Margalit, B., & Metzger, B. D. 2018, ApJL, 868, L4
Massey, P., Neugent, K. F., & Levesque, E. M. 2019, AJ, 157, 227
Matthews, A. M., Condon, J. J., Cotton, W. D., & Mauch, T. 2021, ApJ, 909, 193
McConnell, D., Hale, C. L., Lenc, E., et al. 2020, PASA, 37, e048
Mckinven, R., Gaensler, B. M., Michilli, D., et al. 2023, ApJ, 951, 82
McMullin, J. P., Waters, B., Schiebel, D., Young, W., & Golap, K. 2007, in ASP Conf. Ser. 376, CASA Architecture and Applications, ed. R. A. Shaw, F. Hill, & D. J. Bell (San Francisco, CA: ASP), 127
Mena-Parra, J., Leung, C., Cary, S., et al. 2022, AJ, 163, 48
Metzger, B. D., Berger, E., & Margalit, B. 2017, ApJ, 841, 14
Metzger, B. D., Margalit, B., & Sironi, L. 2019, MNRAS, 485, 4091
Michilli, D., Bhardwaj, M., Brar, C., et al. 2023, ApJ, 950, 134
Michilli, D., Masui, K. W., Mckinven, R., et al. 2021, ApJ, 910, 147
Michilli, D., Seymour, A., Hessels, J. W. T., et al. 2018, Natur, 553, 182
Mohan, N., & Rafferty, D., 2015 PyBDSF: Python Blob Detection and Source Finder, Astrophysics Source Code Library, ascl:1502.007
Mooley, K. P., Hallinan, G., Bourke, S., et al. 2016, ApJ, 818, 105
Murase, K., Kashiyama, K., & Mészáros, P. 2016, MNRAS, 461, 1498
Murphy, E. J., Condon, J. J., Schinnerer, E., et al. 2011, ApJ, 737, 67
Nimmo, K., Chatterjee, S., & Petroff, E. 2023, Fast Radio Burst Community Newsl., 4
Nimmo, K., Hewitt, D. M., Hessels, J. W. T., et al. 2022, ApJL, 927, L3
Niu, C. H., Aggarwal, K., Li, D., et al. 2022, Natur, 606, 873
Nunez, C., Tejos, N., Pignata, G., et al. 2021, A&A, 653, A119
Offringa, A. R., de Bruyn, A. G., Zaroubi, S., & Biehl, M. 2010, arXiv:1007.2089
Perley, R. A., & Butler, B. J. 2017, ApJS, 230, 7
Pettini, M., & Pagel, B. E. J. 2004, MNRAS, 348, L59
Planck Collaboration, Aghanim, N., Akrami, Y., et al. 2020, A&A, 641, A6
Platts, E., Weltman, A., Walters, A., et al. 2019, PhR, 821, 1
Pleunis, Z., Good, D. C., Kaspi, V. M., et al. 2021, ApJ, 923, 1
Prochaska, J., Hennawi, J., Westfall, K., et al. 2020, JOSS, 5, 2308
Rajwade, K. M., Bezuidenhout, M. C., Caleb, M., et al. 2022, MNRAS, 514, 1961
Ravi, V., Catha, M., Chen, G., et al. 2023, ApJL, 949, L3
Reddy, N., Dickinson, M., Elbaz, D., et al. 2012, ApJ, 744, 154
Reddy, N. A., Steidel, C. C., Fadda, D., et al. 2006, ApJ, 644, 792
Resmi, L., Ishwara-Chandra, C. H., Castro-Tirado, A. J., et al. 2005, A&A, 440, 477
Rhodes, L., Caleb, M., Stappers, B. W., et al. 2023, MNRAS, 525, 3626
Ryan, G., van Eerten, H., Piro, L., & Troja, E. 2020, ApJ, 896, 166
Rybicki, G. B., & Lightman, A. P. 1986, Radiative Processes in Astrophysics (New York: Wiley)
Schlegel, D. J., Finkbeiner, D. P., & Davis, M. 1998, ApJ, 500, 525
Science Software Branch at STScI, 2012 PyRAF: Python alternative for IRAF, Astrophysics Source Code Library, ascl:1207.011
Seymour, N., Dwelly, T., Moss, D., et al. 2008, MNRAS, 386, 1695
Shimwell, T. W., Hardcastle, M. J., Tasse, C., et al. 2022, A&A, 659, A1
Spitler, L. G., Scholz, P., Hessels, J. W. T., et al. 2016, Natur, 531, 202
Sridhar, N., & Metzger, B. D. 2022, ApJ, 937, 5
Sridhar, N., Metzger, B. D., Beniamini, P., et al. 2021, ApJ, 917, 13
Sridhar, N., Metzger, B. D., & Fang, K. 2024, ApJ, 960, 74
Stern, D., Assef, R. J., Benford, D. J., et al. 2012, ApJ, 753, 30
Stratta, G., Gendre, B., Atteia, J. L., et al. 2013, ApJ, 779, 66
Tabatabaei, F. S., Schinnerer, E., Krause, M., et al. 2017, ApJ, 836, 185
Tendulkar, S. P., Bassa, C. G., Cordes, J. M., et al. 2017, ApJL, 834, L7
Theureau, G., Hanski, M. O., Coudreau, N., Hallet, N., & Martin, J. M. 2007, A&A, 465, 71
Trouille, L., Barger, A. J., & Tremonti, C. 2011, ApJ, 742, 46
Vohl, D., Vedantham, H. K., Hessels, J. W. T., et al. 2023, A&A, 680, A98
Williams, P. K. G., Clavel, M., Newton, E., & Ryzhkov, D., 2017 pwkit: Astronomical Utilities in Python, Astrophysics Source Code Library, ascl:1704.001
Wright, E. L., Eisenhardt, P. R. M., Mainzer, A. K., et al. 2010, AJ, 140, 1868
Yan, Z., Yu, W., Page, K. L., et al. 2024, ApJ, submitted
Yang, Y.-P., Li, Q.-C., & Zhang, B. 2020, ApJ, 895, 7
Yang, Y.-P., Zhang, B., & Dai, Z.-G. 2016, ApJL, 819, L12
Zhang, B. 2020, Natur, 587, 45
Zhang, X., Yu, W., Law, C., et al. 2023, ApJ, 959, 89